RSC Advances

PAPER

View Article Online
View Journal | View Issue

Cite this: *RSC Adv.*, 2026, **16**, 15640

A green tandem cyclization approach to substituted 2-aminothiazoles *via* molecular sieve/I_2 catalysis: DFT, molecular dockings, and pharmacokinetic profiles

Goncagül Serdaroğlu, *[a] Nesimi Uludag [b] and Elvan Üstün[c]

In an effort to promote eco-friendly organic synthesis, a facile, sustainable, and highly efficient procedure for the synthesis of 2-amino-1,3-thiazole derivatives was developed. The protocol of this process incorporates the principles of green chemistry. Moreover, the NMR, FT-IR, and UV simulations of the compounds were conducted at the B3LYP/6-311++G** level for comparison with the observed counterparts. FMO analyses revealed that the PhTA compound exhibited the highest stability *via* back-donation; among the compounds, NapTA exhibited the lowest stability *via* back-donation. Furthermore, the $-NH_2$ group did not influence electrophilic attacks because the LUMO for all compounds did not separate from this group. Also, the lipophilicity, solubility, pharmacokinetics, and drug-likeness profiles of the compounds were evaluated. The BOILED-Egg model implied that the compounds PhTA, BFTA, and NapTA permeate through the BBB (blood–brain-barrier) passively, while the FTA and ThTA compounds have no potency in terms of BBB penetration. Also, all compounds met the requested physicochemical criteria according to the Lipinski, Veber, and Egan rules. Additionally, the molecules were analyzed using the molecular docking method to gain insights into their possible anticancer activity. Vascular endothelial growth factor receptor-2, human estrogen receptor, human cytochrome P450, and human extracellular signal-regulated kinase 2 were selected. All the obtained results are expected to provide important insights into the structure–reactivity relationship in early-stage drug design research.

Received 23rd December 2025
Accepted 5th March 2026

DOI: 10.1039/d5ra09930g

rsc.li/rsc-advances

1. Introduction

2-Aminothiazole is a heterocyclic aromatic amine characterized by a thiazole core, a five-membered ring system containing sulfur and nitrogen at the 1,3-positions, substituted with various functional groups.[1] The thiazole ring is a main structural motif and is applied extensively in different natural compounds, such as pharmaceutical drugs, biocides, and fungicides.[2] Moreover, thiazole derivatives are well known for their diverse biological activities and have been documented to exhibit both antimycobacterial and antiplasmodial effects. Molecules incorporating the 2-amino-4-(2-pyridyl)thiazole scaffold are of particular significance, especially when the amino group is substituted with aryl or aryl-alkyl functionalities.[3,4] Consequently, considerable efforts have been devoted to developing methods for the synthesis of 2-aminothiazoles.[5,6] Although numerous studies on the synthesis of 2-aminothiazoles have been reported in the literature, to the best of our knowledge, no research has focused on developing an environmentally friendly and efficient one-pot procedure for their synthesis using a green catalyst. In this work, we describe a concise, rapid, and efficient method for preparing aminothiazole derivatives through a one-pot reaction of various ketones with thiourea in the presence of ethanol and molecular sieves under reflux conditions (Scheme 1).[7]

Molecular docking, which predicts the details of the interactions between drug-candidate small molecules and larger target molecules, is a crucial computational technique in drug discovery and biochemistry. This technique not only suggests the binding types, sites, and orientation of the interactions but also assists in revealing the action mechanisms of drug candidates.[8] Additionally, this method reduces the time and labor costs of drug discovery studies. On the other hand, correct target selection can provide reliable binding predictions and selectivity.[9] In this study, vascular endothelial growth factor receptor-2 (VEGFR-2),[10] human estrogen receptor,[11] human cytochrome P450,[12] and human extracellular signal-regulated kinase 2 (ERK2)[13] were selected as target molecules to analyze the possible anticancer activities of the molecules.

[a]*Sivas Cumhuriyet University, Faculty of Education, Math. and Sci. Edu., Sivas, 58140, Turkey. E-mail: goncagul.serdaroglu@gmail.com*

[b]*Department of Chemistry, Faculty of Arts and Sciences, Namık Kemal University, Tekirdağ, 59030, Turkey. E-mail: nuludag@nku.edu.tr*

[c]*Department of Chemistry, Faculty of Art and Science, Ordu University, 52200 Ordu, Turkey. E-mail: elvanustun77@gmail.com*

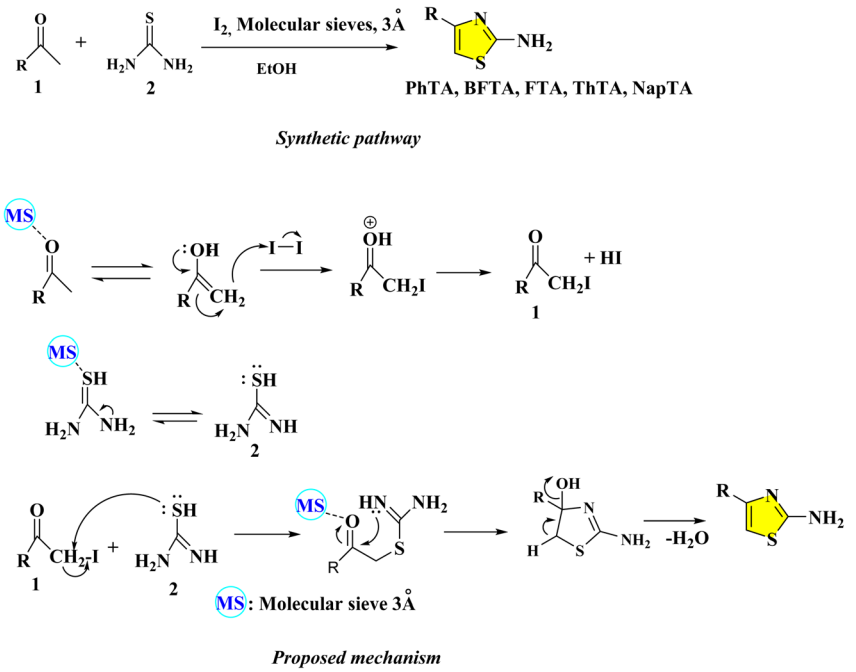

Scheme 1 Synthetic pathway and proposed mechanism for 2-amino-1,3-thiazole derivatives.

Recently, the optical absorption spectra of functionalized cyclopropylthiazole derivatives were investigated by using PBE0/6-311++G(d,p) level computations to elucidate the electronic characteristics.[14] Moreover, halogen-substituted phenylthiazoleamine derivatives were explored for their α-glucosidase inhibition potency, and B3LYP/6-311G(d,p) simulations were performed to elucidate the possible reactivity tendencies of the compounds.[15] In research developing the synthetic methodology, the photochemical behavior of 2-aminothiazole derivatives was evaluated with DFT simulations to gain a deep understanding of the key electronic features underlying the phototransformations.[16] Recently, the UV-induced photodegradation of 2-aminothiazole-4-carboxylic acid derivatives was investigated using B3LYP-D3/6-311++G(3df,3pd) to determine photolysis pathways.[17] Additionally, the newly synthesized and characterized aminothiazole-based dyes were investigated using B3LYP/6-311G** and Cam-B3LYP 6-311 G++(d,p) levels to explore the electronic and UV-Vis characteristics of the data set.[18] Moreover, a series of *N*-(thiazol-2-yl)piperidine-2,6-dione derivatives were prepared and characterized by X-ray crystallography; then, SHG "second-harmonic-generation" features were explored: UV spectroscopic computations were performed to verify the SHG phenomenon.[19] Two new 2-naphthol-thiazole-azo compounds were synthesized and investigated for their anticancer and antioxidant potencies; DFT/B3LYP/6-31+G (d) computations were performed to elucidate the reactivity behaviors.[20]

Herein, the combined experimental and theoretical studies of the compounds (Scheme 2) were performed to synthesize 2-aminothiazoles *via* a green pathway; then, *in silico* simulations were performed to predict and evaluate the electronic, spectroscopic, and physicochemical behaviors as well as the molecular dockings.

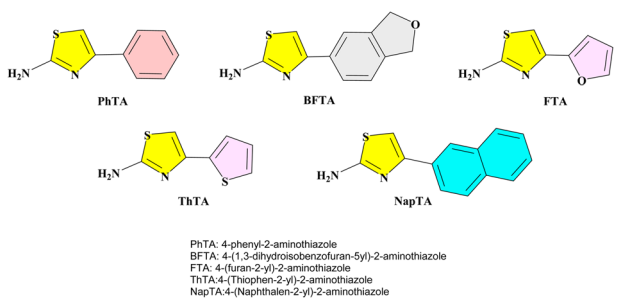

Scheme 2 Chemical structures of 2-aminothiazoles.

2. Experimental and computational methods

2.1. Materials and measurement

The ^{1}H and ^{13}C NMR spectra were obtained using a Bruker instrument DPX-400 MHz High Performance Digital FT-NMR Spectrometer in $CDCl_3$ and DMSO-d_6 as solvents, with tetramethyl silane (TMS) as the internal standard at 25 °C. Chemical shifts (δ) are reported in parts per million (ppm), and coupling constants (J) are reported in hertz (Hz). FT-IR spectra were recorded on a Matson-1000 spectrophotometer using KBr pellets within the 400–4000 cm^{-1} wavenumber range. Melting points were determined using a Gallenkamp apparatus and capillary tubes. The UV spectrum was measured using Shimadzu UV-vis spectrophotometer 2600. Reaction progress was monitored by thin-layer chromatography (TLC) on silica gel 60 F_{254} plates. All reagents and solvents were obtained from

commercial sources, and reactions were carried out under a nitrogen atmosphere after proper solvent purification.

2.2. General procedure for the preparation of the synthesis of reagents and products

2.2.1. General procedure for the synthesis of 2-aminothiazole derivatives. A mixture of acetophenone **1** (600 mg, 5 mmol), iodine (400 mg, 5 mmol), and molecular sieves (3 Å, 10.0 g) in anhydrous 50 mL of EtOH was refluxed for 1 h, and the progress of the reaction was monitored by TLC. After completion, thiourea **2** (380 mg, 5 mmol) was added, and the mixture was further refluxed for 1 h in a nitrogen atmosphere. After completion of the reaction, the mixture was allowed to cool to room temperature, and the solvent was removed under reduced pressure. The resulting residue was extracted with EtOAc, followed by extraction and washing with 10% Na_2SO_3 solution. The residue was diluted with 30 mL of 10% $NaHCO_3$ solution and extracted with ethyl acetate. Purification of the residue by silica gel chromatography using chloroform as the eluent afforded the expected products PhTA (94%), BFTA (86%), FTA (78%), ThTA (75%), and NapTA (67%) in yield.

2.2.2. 4-Phenyl-2-aminothiazole (PhTA). White solid, 827 mg yield 94%, mp: 151–152 °C, R_f 0.33 (EtOAc). UV (MeOH), λ_{max} 280, 332 nm. IR spectrum (KBr, ν): 3430, 3241, 3121, 1591, 1523, 1477, 1442, 1334, 1301, 1193, 1068, 1032, and 1024 cm^{-1}. ^1H NMR (400 MHz, $CDCl_3$): δ = 5.48 and 5.59 (2s, 2H), 6.85 (s, 1H), 7.28 (dd, 1H, J = 7.6 Hz), 7.35 (t, 2H, J = 7.4 Hz), and 7.75 (d, 2H, J = 7.8 Hz); ^{13}C NMR (100 MHz, $CDCl_3$): δ = 101.6, 124.4, 126.9, 127.5, 128.3, 129.3, 135.5, 152.1, and 168.4.

Found, %: C, 61.27; H, 4.64; and N, 15.82. $C_9H_8N_2S$. Calcd, %: C, 61.34; H, 4.58; and N, 15.90.

2.2.3. 4-(1,3-Dihydroisobenzofuran-5-yl)-2-aminothiazole (BFTA). White solid, 937 mg, yield 86%, mp: 114–116 °C, R_f 0.28 (EtOAc). UV (MeOH), λ_{max} 322, 438 nm. IR spectrum (KBr, ν): 3435, 3289, 3119, 1923, 1634, 1532, 1493, 1480, 1443, 1323, 1296, 1243, 1192, 1123, and 1035 cm^{-1}. ^1H NMR (400 MHz, DMSO-d_6): δ = 3.43 (s, 4H), 6.11 (s, 2H), 6.85-6.94 (m, 1H), 7.02 (s, 2H), and 7.33 (s, 1H); ^{13}C NMR (100 MHz, DMSO-d_6): δ = 101.1, 102.1, 104.9, 107.3, 118.4, 128.5, 145.4, 146.2, 148.1, 148.5, and 167.1.

Found, %: C, 60.44; H, 4.57; and N, 12.94. $C_{11}H_{10}N_2OS$. Calcd, %: C, 60.53; H, 4.62; and N, 12.83.

2.2.4. 4-(Furan-2-yl)-2-aminothiazole (FTA). White solid, 714 mg, yield 86%, mp: 125–126 °C, R_f 0.51 (EtOAc). UV (MeOH), λ_{max} 254, 334 nm. IR spectrum (KBr, ν): 3431, 3268, 3108, 2962, 1631, 1524, 1452, 1381, 1324, 1211, 1148, 1041, 1002, and 801 cm^{-1}. ^1H NMR (400 MHz, DMSO-d_6): δ = 6.51 (d, 2H, J = 4.7 Hz), 6.73 (s, 1H), 7.10 (s, 2H), and 7.62 (s, 1H); ^{13}C NMR (100 MHz, DMSO-d_6): δ = 101.5, 105.0, 112.6, 140.8, 141.2, 151.6, and 167.6.

Found, %: C, 50.64; H, 3.57; and N, 16.93. $C_7H_6N_2OS$. Calcd, %: C, 50.59; H, 3.64; and N, 16.86.

2.2.5. 4-(Thiophen-2-yl)-2-aminothiazole (ThTA). White solid, 698 mg, yield 75%, mp: 134–135 °C, R_f 0.41 (EtOAc). UV (Me), λ_{max} 309, 341 nm. IR spectrum (KBr, ν): 3342, 3260, 2921, 1627, 1554, 1518, 1361, 1321, 1283, 1077, and 1048 cm^{-1}. ^1H NMR (400 MHz, $CDCl_3$): δ = 5.53 (s, 2H), 6.58 (s, 1H), 7.01 (t, 1H, J = 4.7 Hz), 7.20 (d, 1H, J = 4.5 Hz), and 7.30 (d, 1H, J = 3.4 Hz); ^{13}C NMR (100 MHz, $CDCl_3$): δ = 102.2, 122.5, 123.4, 127.5, 137.5, 144.3, and 166.6.

Found, %: C, 46.19; H, 3.28; N, and 15.31. $C_7H_6N_2S_2$. Calcd, %: C, 46.13; H, 3.32; and N, 15.37.

2.2.6. 4-(Naphthalen-2-yl)-2-aminothiazole (NapTA). White solid, 758 mg, yield 67%, mp: 157–158 °C, R_f 0.33 (EtOAc). UV (MeOH), λ_{max} 314, 348 nm. IR spectrum (KBr, ν): 3421, 3244, 3121, 2922, 1621, 1589, 1523, 1493, 1358, 1327, 1180, and 1031 cm^{-1}. ^1H NMR (400 MHz, DMSO-d_6): δ = 7.10 (s, 2H), 7.48–7.52 (m, 2H), 7.87–7.97 (m, 5H), and 8.35 (s, 1H); ^{13}C NMR (100 MHz, DMSO-d_6): δ = 101.5, 123.1, 124.8, 125.8, 126.4, 126.8, 127.5, 127.9, 128.1, 131.3, 132.1, 148.8, and 167.2.

Found, %: C, 60.06; H, 4.39; and N, 12.27. $C_{13}H_{10}N_2S$. Calcd, %: C, 69.00; H, 4.45; and N, 12.38.

2.3. Molecular docking methods

VEGFR-2 (pdb: 1ywn),[21] human estrogen receptor (pdb: 3ert),[22] human cytochrome P450 (pdb: 3ruk),[23] and human ERK2 (pdb: 4qta)[24] crystal structures were downloaded from the RCSB protein data bank (https://www.rcsb.org/). AutoDockTools 4.2 was used for all molecular docking performances.[25,26] The biomacromolecules were first recorded in pdbqt format, which was used as rigid molecules during the performances. The polar hydrogens and Kollman charges were evaluated, while the water molecules were removed from the target molecules before the processes in which Lamarckian genetic algorithms, such as 150, were considered.[27,28] The 2-aminothiazole-type molecules were also recorded as pdbqt using Gasteiger charges.[29] All the illustrations of the results were drawn and prepared using Discovery Studio 4.1.0.

2.4. DFT studies

B3LYP[30,31]/6-311++G** level[32] simulations of the compounds were performed using G16W[33] by default settings.[34,35] The visualizations of the quantum chemical computations were made using GaussView 6.0.16 (ref. 36) software. The calculated vibrational modes of the compounds were scaled down by 0.96 (high) and 0.988 (low) to make them comparable to the experimental modes.[37] The NMR shifts were calculated at the same level of the theory using the GIAO "Gauge-Independent Atomic Orbital"[38,39] method in the related simulation media depending on the observed media. Furthermore, the TD-DFT/B3LYP/6-311++G** level[40,41] simulations were performed in the methanol phase, which was the solvent used in recording the experimental spectra. The PCM (polarizable continuum model)[42,43] was used to simulate the related solvent media in this work. The basis of statistical mechanics principles was used to predict and evaluate the thermochemical and physicochemical data of the synthesized compounds.[44–46]

The global reactivity parameters obtained from I (ionization energy) and A (electron affinity)[47] resulted in the following equations:

$$I = -E_{HOMO},$$

Table 1 Physicochemical properties

	PhTA	BFTA	FTA	ThTA	NapTA
Formula	$C_9H_8N_2S$	$C_{11}H_{10}N_2OS$	$C_7H_6N_2OS$	$C_7H_6N_2S_2$	$C_{13}H_{10}N_2S$
MW (g mol^{-1})	176.24	218.27	166.20	182.27	226.30
Num. HA	12	15	11	11	16
Num. AHA	11	11	10	10	15
Fraction Csp^3	0.00	0.18	0.00	0.00	0.00
Num. RB	1	1	1	1	1
Num. HBA	1	2	2	1	1
Num. HBD	1	1	1	1	1
Molar ref.	51.95	60.86	44.22	49.83	69.46
TPSA (Å^2)[a]	67.15	76.38	80.29	95.39	67.15

[a] TPSA, "topological polar surface area"; HBA, "hydrogen bond acceptor"; HBD, "hydrogen bond donor"; RB, "rotatable bonds"; AHA, "aromatic heavy atoms"; and Ref, "refractivity".

$$A = -E_{\mathrm{LUMO}},$$

$$\chi = -\left(\frac{I + A}{2}\right),$$

$$\eta = \frac{I - A}{2},$$

$$\omega = \frac{\mu^2}{2\eta},$$

$$\Delta N_{\max} = \frac{I + A}{2(I - A)},$$

$$\omega^+ \approx (I + 3A)^2/(16(I - A)),$$

$$\omega^- \approx (3I + A)^2/(16(I - A)),$$

$$\Delta\varepsilon_{\text{back-donation}} = -\frac{\eta}{4},$$

where χ denotes the electronic chemical potential, η denotes the global hardness, ω denotes the electrophilicity, $\Delta N_{\max}$ denotes the maximum charge transfer capability index,[48–53] ω denotes the electron-donating power, ω^+ denotes the electron-accepting power,[54] and $\Delta E_{\text{back-donat.}}$ denotes the back-donation energy.[55]

2.5. Physicochemistry, ADMET, and druglikeness

The LOGP "lipophilicity", LOGS "water-solubility", pharmacokinetics profiles, and drug-likeness features of synthesized compounds PhTA, BFTA, FTA, ThTA, and NapTA were calculated using SwissADME[56] tools. Herein, the LOGP scores of the compounds were evaluated in light of 5 approaches, such as ILOGP,[57] XLOGP3,[58] WLOGP,[59] MLOGP,[60] and SILICO-IT.[61] As is well known, the LOGP value is described as follows:

$$\log P_{\mathrm{o/w}} = \log \frac{C_{\mathrm{o}}}{C_{\mathrm{w}}},$$

where C_{o} denotes the concentrations of the neutral molecule in octanol and C_{w} denotes the concentrations of the neutral molecule in water.

Moreover, the log S values are given by the following formulae:

$$\log S_{\mathrm{w}} = 0.16\text{–}0.63\ c\log P - 0.0062\ \mathrm{MWT} + 0.066\ \mathrm{RB} - 0.74\ \mathrm{AP}\ (\mathrm{ESOL}),[62]$$

$$\log S_{\mathrm{w}} = -1.0239\log P - 0.0148\ \mathrm{TPSA} - 0.0058\ (\mathrm{m.p.\ (C)} - 25) + 0.3295\ \mathrm{aroOHdel} + 0.5337\ (\mathrm{ALI}).[63]$$

The terms are described as MWT "molecular weight", RB "rotatable bonds", AP "aromatic proportion", TPSA "topological surface area", aroOHdel "aromatic –OH group number", and MP "melting point".

The drug-likeness properties of the compounds were determined using the Lipinski,[60] Ghose,[64] Veber,[65] Egan,[66] and Muegge[67] approaches. The Abbott[68] index was used to appraise the bioavailability of the data set, whose molecular structure and physicochemical features are depicted in Table 1.

3. Results and discussion

3.1. Synthesis and spectroscopic characterization

The reaction of acetophenone **1** with thiourea **2** was carried out under the conditions described in this study. As part of our ongoing investigation into the use of molecular sieves in heterocyclic synthesis, the same methodology was applied to other substrates under similar conditions. Acetophenone **1** was selected as the model compound for the optimization of the reaction parameters. To determine the most suitable solvent, a series of reactions was performed using different solvents. The results are summarized in Table 2. Among the solvents tested, ethanol proved to be the most effective. In the presence of molecular iodine, molecular sieves, and thiourea **2**, acetophenone **1** was efficiently converted to the desired product in 94% yield after refluxing for 2 h (Table 2, entry 8). Reactions conducted under reflux consistently afforded higher yields than

Table 2 Optimization of reaction conditions

Entry	**1** (equiv.)	**2** (equiv.)	Solvents	Conditions	Yield (%)
1	1.0	1.0	THF	25 °C	27
2	1.0	1.0	THF	Reflux	41
3	1.0	1.0	DMF	25 °C	44
4	1.0	1.0	DMF	Reflux	51
5	1.0	1.0	MeCN	25 °C	47
6	1.0	1.0	MeCN	Reflux	63
7	1.0	1.0	EtOH	25 °C	51
8	1.0	1.0	**EtOH**	**Reflux**	**94**
9	1.0	3.0	EtOH	Reflux	93
10	1.0	1.0	MeOH	25 °C	51
11	1.0	1.0	MeOH	Reflux	87
12	1.0	1.0	Dioxane	25 °C	55
13	1.0	1.0	Dioxane	Reflux	64
14	1.0	1.0	Toluene	25 °C	44
15	1.0	1.0	Toluene	Reflux	67
16	1.0	1.0	DMSO	25 °C	38
17	1.0	1.0	DMSO	Reflux	61
18	1.0	1.0	CH_2Cl_2	25 °C	35
19	1.0	1.0	CH_2Cl_2	Reflux	48

those performed at room temperature. Reaction progress was monitored using thin-layer chromatography (TLC). Upon completion, the mixture was treated with 30 mL of 10% $NaHCO_3$ solution and extracted with ethyl acetate. The combined organic layers were dried over $MgSO_4$, and the solvent was removed under reduced pressure to afford the crude product (see the Experimental section). Other solvents, including THF, DMF, MeCN, MeOH, dioxane, toluene, DMSO, and CH_2Cl_2, were also evaluated but were significantly less effective than ethanol. Consequently, ethanol was identified as the optimal solvent for the synthesis of the corresponding products (PhTA, BFTA, FTA, ThTA, and NapTA). Subsequently, different molar ratios of the reactants were examined. A 1 : 1 molar ratio provided the highest yield, and increasing the amount of thiourea **2** to three equivalents did not improve the outcome. Therefore, the optimal conditions for PhTA formation were established as refluxing equimolar amounts of acetophenone **1** and thiourea **2** in ethanol (Table 2, entry 8). The structure of the synthesized compound was confirmed by ^{1}H and ^{13}C NMR as well as IR spectroscopy. An examination of the proton NMR spectra showed that the NH_2 signals at 5.48 and 5.59 ppm in the ^{1}H NMR spectrum were associated with the PhTA structure. For BFTA, the resonance observed at 6.11 ppm was assigned to the NH_2 group, while the signal at 3.43 ppm was attributed to the CH_2 protons. The synthesized compounds were also confirmed by analyzing their FT-IR and ^{13}C NMR spectra. Additionally, a series of substituted 2-aminothiazoles (PhTA, BFTA, FTA, ThTA, and NapTA) was synthesized in good yields, and a plausible reaction mechanism was proposed (Scheme 1). In our previous studies, molecular sieves were employed; in the present study, we further supported green chemistry principles using ethanol as a solvent in combination with molecular sieves. Table 3 provides a comparative analysis of the current methodology against previously reported literature, highlighting differences in catalysts, temperature ranges, and reaction yields.[69–72] This strategy offers a new approach to the synthesis of various aromatic compounds.

Given the broad applications of thiazoles in medicinal chemistry, this method represents an efficient and environmentally friendly synthetic route. Moreover, the protocol proved applicable to the preparation of structurally diverse 2-aminothiazole derivatives from commercially available ketones. Although NapTA was obtained in a relatively lower yield due to the formation of unidentified by-products, this outcome further highlights the synthetic utility of the method, as other aromatic and heterocyclic derivatives were produced in significantly higher yields than the naphthalene analogue.

3.1.1. FT-IR spectra. FT-IR spectroscopy is one of the essential methods for analyzing functional group(s) in relevant molecular systems and plays an important role in synthetic chemistry. In this work, the observed and calculated IR spectra of the synthesized compounds are presented in Fig. S1–S5; the calculated vibrations are summarized in Table S1 (SI data).

Related to the primary amine group, the apparent peaks at 3430 and 3421 cm^{-1} of the PhTA compound were related to the asymmetric and symmetric bond elongation modes of the NH_2 group assigned at 3529 and 3425 cm^{-1}, respectively. Furthermore, the $\nu NH_{2(as.)}$ modes for the BFTA, FTA, ThTA, and NapTA compounds were observed at 3435, 3431, 3342, and 3421 cm^{-1}, respectively, whereas they were assigned at 3531, 3528, 3531, and 3530 cm^{-1}. From Table S1, the apparent peak of the PhTA compound at 3121 cm^{-1} was simulated in the range of 3129-3033 cm^{-1} and related to the C–H bond elongation. The recorded peaks of the PhTA, BFTA, FTA, ThTA, and NapTA compounds at 1591, 1634, 1631, 1627, and 1621 cm-1 of the compounds were calculated at 1628, 1627, 1629, 1628, and 1628 cm^{-1}, respectively, and were related to the NH_2 bending mode. Moreover, the βNH_2 mode and νCC mode of the PhTA compound were calculated and recorded at 1622 and 1523 cm^{-1}, respectively. The νN=C stretching mode for the PhTA compound was assigned and observed at 1559 and

Table 3 Comparison of the synthesis of substituted 2-aminothiazole (PhTA) derivatives

Entry	Catalyst/solvent	Temperature (°C)	Time (h)	Yield[a] (%)	References
1	Ca/4-MePy-IL@ZY-Fe_3O_4/EtOH	80	1.5	90	69
2	Nanochitosan (EtOH)	Reflux (80)	2.5	95	70
3	$FeCl_3 \cdot 6H_2O$ (20 mol%)/PEG-400/CH_3CN	110	24	58	71
4	I_2/DMSO	80	12	53	72
5	Molecular sieve/I_2/EtOH	Reflux	2	94	This study

[a] Isolated yield.

1477 cm^{-1}, respectively, while the νN=C for the NapTA compound was observed and calculated at 1493 and 1558 cm^{-1}. However, the single bond N–H stretching for the BFTA and FTA compounds was recorded at 1443 and 1324 cm^{-1}, respectively, and computed in the ranges of 1331–1286 and 1330–1293 cm^{-1}, respectively. The νC–O modes for the BFTA and FTA compounds were recorded at 1035 and 1041 cm^{-1}, respectively, and assigned at 1061 and 905 as well as at 1229 and 1094 cm^{-1}. Recently, the C–O single bond stretching for pyrrole derivatives was recorded in the range of 1258–1047 cm^{-1} and predicted with the B3LYP/6-311G** level simulations in 1241–1003 cm^{-1}.[7] Additionally, the νN=C stretching for the pyrazine derivatives was calculated by the B3LYP/6-311 G** level in the range of 1581–1110 cm^{-1} (ref. 73) and recorded in 1544–1336 cm^{-1} for the pyrrole derivatives.[7,74] The aromatic C–H bond stretching was recorded at 3099 and 3043 cm^{-1}, which were assigned by PED analysis in 3130 (99% PED) and 3087 cm^{-1} (100% PED), respectively.[75] In previous studies, the νNH mode for dasycarpidone was observed at 3221 cm^{-1} and predicted at 3507 cm^{-1} (100% PED) using B3LYP/6-311 G(d,p) level computations.[76]

3.1.2. ^{13}C NMR and ^{1}H NMR spectra. In synthetic chemistry, NMR spectroscopy is also a key analytical tool that provides deep information about the chemical environment and dynamics of the related systems. The observed ^{1}H and ^{13}C NMR spectra of the compounds are presented in Fig. S6–S10, S11–S15, respectively, in the SI data; the related numerical data of the chemical shifts are presented in Table S2.

For the PhTA compound, the sp^2-hybridized Cs gave peaks of the ^{13}C NMR spectrum in the range of 101.6–168.4 ppm, which were assigned in the range of 114.0–178.1 ppm. Moreover, the largest chemical shifts of the PhTA compound were determined at 168.4 and 152.1 ppm for the C12 and C13 atoms, respectively, bonded to the electronegative N atom, while they were calculated at 178.1 and 157.9 ppm. Similarly, the corresponding C shifts for the BFTA compound were calculated at 179.3 and 157.8 ppm, respectively, and observed at 167.1 and 148.5 ppm. However, the sp^3-hybridized Cs showed peaks at 101.1 (C1) and 102.1 ppm (C3) and were assigned at 80.2 ppm. Furthermore, the C1 shift for the FTA, ThTA, and NapTA compounds appeared at 167.6, 166.6, and 167.2 ppm, respectively, whereas it was predicted at 179,8, 177.8, and 179,6 ppm, respectively, which were the highest C shifts for these compounds due to the presence of the electronegative atom. Additionally, the second-highest shift for the FTA compound was calculated and observed for the C10 atom bonded to the electronegative O atom at 159.6 and 151.6 ppm, respectively. For the FTA compound, the apparent peak at 140.8 ppm was associated with the shift of the C15 atom bonded to the O atom and was calculated at 149.4 ppm. Previously, aromatic C atom shifts, which were neighbors to the N atom, were observed at 128.5 and 138.3 ppm, and assigned at 136.88–145.23 ppm.[77] The Cs shifts of the phenyl carbons for the thiophene derivatives were recorded at 117.4–147.8 ppm and assigned at 130.6–157.7 ppm,[78,79] respectively.

Moreover, the largest proton shift for the PhTA compound appeared at 7.75; then, 7.37 ppm was associated with the H7 and H11 atoms assigned at 8.44 and 8.02 ppm, respectively. Similarly, the chemical shifts for the corresponding Hs of the BFTA compound were recorded at 7.33 ppm (H15, H16), and assigned at 8.25 ppm (H15) and 7.90 ppm (H16). Previously, the ^{1}H shifts in the aromatic ring of the tubifolidine compound were observed at 6.51–7.02 ppm, and simulated at 6.74–7.28 ppm using B3LYP/6-311++G(df,pd) level.[80] The proton shifts of the Hs belonging to the amine group for the PhTA compound showed peaks at 5.48 and 5.59 ppm, which were assigned to 4.45 and 4.88 ppm, respectively. Moreover, the shifts for the H8 and H9 of the compounds FTA and NapTA were calculated at 4.68 and 4.96 ppm as well as at 4.70 and 5.03 ppm, respectively, which were observed at 6.53 ppm and 7.10 ppm.

3.1.3. UV-vis absorption spectra. UV-vis spectroscopy is an analytical technique used to evaluate how much a sample absorbs radiation in the UV-vis region of the spectrum. In our previous studies, we evaluated the DNA and BSA-binding properties of organic molecular systems[81,82] using this technique. Herein, the simulated UV spectra of the compounds were

Table 4 Theoretical UV-vis absorption characteristics in methanol

	Exp. (λ (nm))	State	Transitions	MO%	ΔE (eV)	λ (nm)	f
PhTA	332	**1**	H → L	(89.9%)	2.7516	451	0.0000
	280	**4**	H → L	(96.4%)	4.1275	300	0.2185
BFTA	438	**1**	H → L	(88.0%)	2.7437	452	0.0000
	322	**4**	H → L	(94.1%)	4.0561	306	0.2156
FTA		**1**	H → L	(95.6%)	2.5658	483	0.0000
	334	**3**	H → L	(98.7%)	4.1377	300	0.3356
	254	**5**	H → L + 1	(79.8%)	4.4634	278	0.0029
			H → L + 2	(7.8%)			
ThTA	341	**1**	H → L	(94.2%)	3.5671	348	0.0000
	309	**3**	H → L	(98.1%)	3.9232	316	0.3369
NapTA		**1**	H → L	(78.3%)	2.4270	511	0.0000
			H − 1 → L	(8.8%)			
			H − 1 → L + 1	(5.0%)			
	348	**3**	H → L	(94.6%)	3.6063	344	0.1410
	314	**6**	H → L + 1	(46.1%)	3.9991	310	0.0526
			H − 1 → L	(40.2%)			

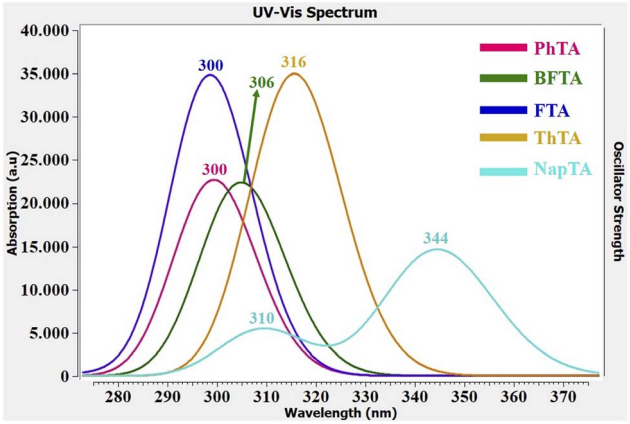

Fig. 1 Simulated UV-vis spectra.

evaluated to provide a deep insight into the nature of the absorption of the radiation of the related compound. The recorded and simulated absorption wavelengths of the compounds are summarized in Table 4; the recorded and simulated electronic spectra of the compounds are depicted in Fig. S16–S20 and 1, respectively.

Accordingly, the first s → s_0 excitation for all compounds was related to the H → L transition even though their oscillator strengths were almost zero. From Fig. 2, the first transitions for the compounds PhTA, FTA, and ThTA were associated with the electron movement from the HOMO expanded on the whole surface to LUMO separated on the surface except for the amine group. However, the H → L transition for BFTA was related to the charge movement from the almost thiazole-amine and partially benzo-part of the dihydroisobenzofuran unit to the whole molecular surface except for the $-NH_2$ group. Furthermore, the recorded peak at 280 nm for the PhTA compound was simulated at 300 nm with $f = 0.2185$ and related to the H → L (96.4%) transition. Similarly, the apparent peaks at 322 nm and 309 nm for the BFTA and ThTA compounds were associated with the H → L interaction determined at 306 and 316 nm, respectively, with oscillator strengths of 0.2156 and 0.3369. Additionally, the recorded shoulder band at 438 nm for the BFTA compound was determined at 452 nm with the MO contribution of 88.0%. However, two peaks recorded at 334 and 254 nm for the FTA compound were predicted at 300 ($f = 3356$) and 278 nm ($f = 0.0029$), respectively; the first peak was related to H → L (98.7%), while the second peak was associated with H → L + 1 (79.8%) and H → L + 2 (7.8%) transitions. Additionally, the recorded peak at 348 nm for the NapTA compound was due to the H → L (94.6%) interaction calculated at 344 nm ($f = 0.1410$), while the second peak apparent at 314 nm was contributed by the H → L + 1 (46.1%) and H − 1 → L (40.2%) transitions simulated at 310 nm ($f = 0.0526$). Herein, all electronic movements for all compounds are due to the n → π* and π → π* transitions (see Fig. 2).

3.2. Molecule structure and physicochemical properties

The structural optimization of the relevant systems is the first step to reliably proceed to further analyses and evaluations. Herein, the optimized structures of the compounds and their calculated structural data are presented in Fig. 3 and Table 5, respectively. Additionally, the fully optimized parameters of the

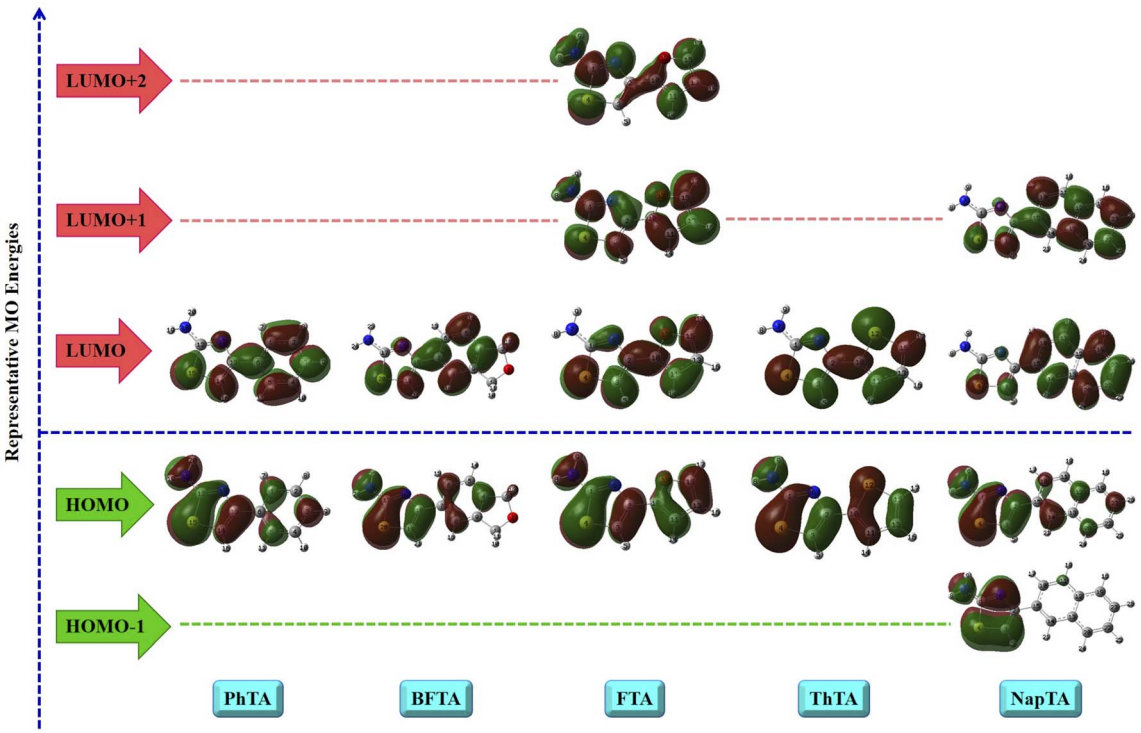

Fig. 2 HOMO and LUMO plots for s → s_0 transitions of the compounds.

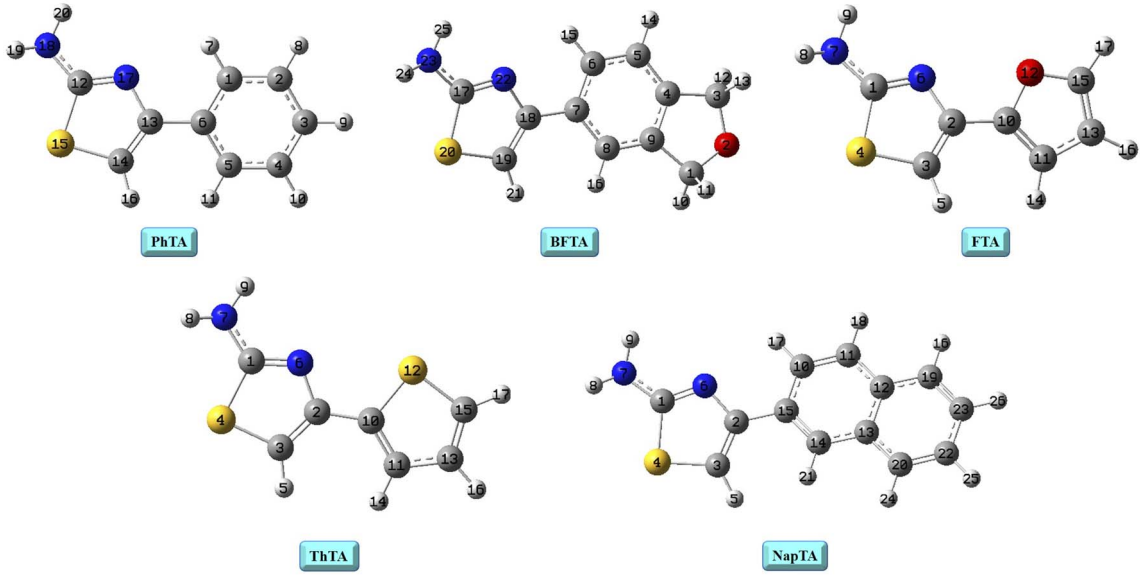

Fig. 3 Optimized structures.

compounds are illustrated in Tables S3–S7 in the SI material of this study.

From Table 5, the S–C bond length that neighbored the N atom in the thiazole ring was calculated to be 1.77 Å for all compounds. Additionally, another S–C bond length in the thiazole ring was determined as 1.74 Å for the PhTA, BFTA, FTA, and NapTA compounds and as 1.75 Å for the ThTA compound. Previously, Toplak and co-workers reported the S–C lengths for the 2-aminothiazole at 1.75 Å and 1.74 Å.[83] Furthermore, the N=C and C–C lengths in the thiazole ring were predicted at 1.38 Å and 1.37 Å, respectively, while they were previously recorded[83] at 1.33 Å and 1.37 Å. However, the atomic distance between the C and N atoms of the amine group was determined herein at 1.38 Å, while the C–NH_2 length for the 2-amino-thiazole was reported at 1.33 Å.[83] The O–C length for BFTA was calculated at 1.43 Å, while this length for FTA was determined at 1.36 Å due to the sp^2 hybridization of the Cs in the furan unit of the compound and thus electron delocalization in the ring. In addition, the C–S–C angles in the thiazole ring for the compounds PhTA, BFTA, FTA, ThTA, and NapTA were calculated at 88.11°, 88.11°, 88.19°, 88.27°, and 88.16°, respectively, while the S–C=C bond angles for the compounds were determined at 110.66°, 110.62°, 110.14°, 110.30°, and 110.56°, respectively. In previous studies, the C–S–C and S–C=C angles for the substituted benzo[*d*]thiazol compound were recorded at 89.39° and 109.14°,[84] respectively. The S–C=N angles for PhTA, BFTA, FTA, ThTA, and NapTA were estimated at 114.70°, 114.72°, 114.85°, 114.67°, and 114.70°, respectively, with deviations of 1.28°, 1.26°, 1.13°, 1.31°, and 1.28° from the reported value of 115.98°.[83] The S–C–N, C=C–N, C–N=C, and N–C–N angles of the PhTA were computed at 121.07°, 114.79°, 111.75°, and 124.12°, respectively, while these angles for NapTA were determined at 121.14°, 114.92°, 111.66°, and 124.08°, respectively. The calculated data agreed with the recorded data of the structurally related compounds.

Table 5 Selected optimized parameters in the gas

Bond length (Å)	Exp.[a]	PhTA	BFTA	FTA	ThTA	NapTA
S–C (=N)	1.75[b]	1.77	1.77	1.77	1.77	1.77
S–C (=C)	1.74[b]	1.74	1.74	1.74	1.75	1.74
N=C (–S)	1.30[c]	1.30	1.30	1.30	1.30	1.30
C–NH_2	1.33[b]	1.38	1.38	1.38	1.38	1.38
C–C (in TA ring)	1.37[b]	1.37	1.37	1.37	1.37	1.37
O–C		—	1.43	1.36	—	—
Bond angle (°)						
S–C=N	115.98[c]	114.70	114.72	114.85	114.67	114.70
C–S–C (in TA)	89.39[c]	88.11	88.11	88.19	88.27	88.16
S–C–NH_2	119.43[b]	121.07	121.12	121.06	121.17	121.14
S–C=C	109.14[c]	110.66	110.62	110.14	110.30	110.56
C=C–N	114.90[b]	114.79	114.85	115.58	115.19	114.92
C–N=C	112.25[b]	111.75	111.71	111.22	111.57	111.66
N–C–NH_2	123.15[b]	124.12	124.09	123.96	124.06	124.08
C–O–C		—	110.45	107.38	—	—
C–S–C		—	—	—	91.57	—

[a] The experimental values are taken from previous reports. [b] Ref. 83. [c] Ref. 84.

Moreover, Table 6 displays the calculated thermochemical parameters, dipole moments, and polarizability values of the verified structures of the compounds. In the gas phase, the ΔE values of the compounds PhTA, BFTA, FTA, ThTA, and NapTA were determined at −855.466389, −1008.093775, −853.273957, −1176.263149, and −1009.097559 au, respectively. Additionally, the ΔG values of the FTA and ThTA compounds were calculated as −853.309760 and −1176.300081 au, respectively, in gas. From Table 6, the thermal energies of the compounds decreased as the solvent dielectric constant increased, from the gas to DMSO media, except for NapTA. Moreover, the $E_{\text{therm.}}$ (in kcal mol^{-1}) value order of PhTA was calculated as gas (101.823) > chloroform (101.726) > methanol (101.699) > DMSO (101.698), while the $E_{\text{therm.}}$ (in kcal mol^{-1}) for NapTA was

Table 6 Thermochemistry and physicochemical values

		PhTA	BFTA	FTA	ThTA	NapTA
Gas ($\varepsilon = 0.0$)	ΔE (au)	−855.466389	−1008.093775	−853.273957	−1176.263149	−1009.097559
	ΔH (au)	−855.455365	−1008.080143	−853.263670	−1176.252360	−1009.083918
	ΔG (au)	−855.503218	−1008.134162	−853.309760	−1176.300081	−1009.137593
	$E_{\text{therm.}}$ (kcal mol^{-1})	101.823	128.070	82.272	80.519	132.620
	C_v (cal mol^{-1} K^{-1})	39.606	49.317	35.740	37.654	51.403
	S (cal mol^{-1} K^{-1})	100.716	113.692	97.005	100.438	112.969
	μ (D)	1.85	3.36	1.48	1.84	1.92
	α (au)	144.35	172.08	123.95	139.60	203.27
Chloroform ($\varepsilon = 4.71$)	ΔE (au)	−855.473444	−1008.102644	−853.282474	−1176.270651	−1009.105486
	ΔH (au)	−855.462415	−1008.089063	−853.272179	−1176.259844	−1009.091781
	ΔG (au)	−855.510207	−1008.142708	−853.318157	−1176.307455	−1009.145953
	$E_{\text{therm.}}$ (kcal mol^{-1})	101.726	128.001	82.139	80.411	132.476
	C_v (cal mol^{-1} K^{-1})	39.663	49.361	35.848	37.746	51.529
	S (cal mol^{-1} K^{-1})	100.589	112.905	96.768	100.205	114.014
	μ (D)	2.36	4.03	2.09	2.42	2.40
	α (au)	181.51	214.21	154.19	176.71	258.10
	$\Delta E_{\text{sol.}}$/(kJ mol^{-1})	18.52	23.29	22.36	19.70	20.81
	$\Delta H_{\text{sol.}}$/(kJ mol^{-1})	18.51	23.42	22.34	19.65	20.64
	$\Delta G_{\text{sol.}}$/(kJ mol^{-1})	18.35	22.44	22.05	19.36	21.95
Methanol ($\varepsilon = 32.61$)	ΔE (au)	−855.476391	−1008.106316	−853.286083	−1176.273784	−1009.108753
	ΔH (au)	−855.465367	−1008.092735	−853.275772	−1176.262974	−1009.095066
	ΔG (au)	−855.513050	−1008.146398	−853.321872	−1176.310792	−1009.149102
	$E_{\text{therm.}}$ (kcal mol^{-1})	101.699	127.968	82.084	80.380	132.462
	C_v (cal mol^{-1} K^{-1})	39.670	49.386	35.892	37.756	51.510
	S (cal mol^{-1} K^{-1})	100.358	112.945	97.025	100.643	113.728
	μ (D)	2.59	4.28	2.41	2.69	2.60
	α (au)	198.33	233.46	167.64	193.73	282.90
	$\Delta E_{\text{sol.}}$/(kJ mol^{-1})	26.26	32.93	31.84	27.92	29.39
	$\Delta H_{\text{sol.}}$/(kJ mol^{-1})	26.26	33.06	31.77	27.87	29.27
	$\Delta G_{\text{sol.}}$/(kJ mol^{-1})	25.81	32.13	31.80	28.12	30.22
DMSO ($\varepsilon = 46.83$)	ΔE (au)	−855.476569	−1008.106537	−853.286305	−1176.273973	−1009.108947
	ΔH (au)	−855.465545	−1008.092956	−853.275991	−1176.263163	−1009.095263
	ΔG (au)	−855.513225	−1008.146627	−853.322131	−1176.310973	−1009.149278
	$E_{\text{therm.}}$ (kcal mol^{-1})	101.698	127.966	82.080	80.378	132.463
	C_v (cal mol^{-1} K^{-1})	39.670	49.387	35.895	37.756	51.506
	S (cal mol^{-1} K^{-1})	100.350	112.962	97.110	100.625	113.683
	μ (D)	2.60	4.30	2.43	2.71	2.61
	α (au)	199.38	234.68	168.48	194.80	284.47
	$\Delta E_{\text{sol.}}$/(kJ mol^{-1})	26.73	33.51	32.42	28.42	29.90
	$\Delta H_{\text{sol.}}$/(kJ mol^{-1})	26.73	33.64	32.35	28.36	29.79
	$\Delta G_{\text{sol.}}$/(kJ mol^{-1})	26.27	32.73	32.48	28.60	30.68

calculated in the order of gas (132.620) > chloroform (132.476) > DMSO (132.463) > methanol (132.462). However, the heat capacity of the compounds increased as the solvent dielectric constant increased, except for the NapTA compound. The C_v (in cal mol^{-1} K^{-1}) orders of FTA and NapTA compounds were determined as gas (35.740) > chloroform (35.848) > methanol (35.892) > DMSO (35.895) and gas (51.403) > DMSO (51.506) > methanol (51.510) > chloroform (51.529), respectively. Furthermore, the S (in cal mol^{-1} K^{-1}) value of the PhTA compound decreased as the solvent dielectric constant increased, and the order was determined as gas (100.716) > chloroform (100.589) > methanol (100.358) > DMSO (100.350). However, the S (in cal mol^{-1} K^{-1}) value changed in the following order: gas (113.692) > DMSO (112.962) > methanol (112.945) > chloroform (112.905), which implied that the BFTA behaved more spontaneously in the gas phase and *vice versa* for the chloroform phase. Unlike BFTA, the NapTA compound behaved more randomly in chloroform media according to the calculated order of chloroform > M > DMSO > gas, and *vice versa* for the gas phase. Herein, it is important to recall that the greatest contribution to the entropy came from the vibrational freedom of the system; the highest entropy value was calculated for the NapTA compound in all simulation media due to having the highest number of atoms and thus the highest number of vibrational modes among the compounds. For instance, the entropy orders in the gas and DMSO phases were predicted as NapTA (112.969) > BFTA (113.692) > PhTA (100.716) > ThTA (100.438) > FTA (97.005) and NapTA (113.683) > BFTA (112.962) > ThTA (100.625) > PhTA (100.350) > FTA (97.110), respectively. From Table 6, both dipole moment and polarizability values increased with an increase in the dielectric constant of the solvent media. The μ (in D) of FTA and ThTA compounds were calculated as follows: gas (1.48) > chloroform (2.09) > methanol (2.41) > DMSO (2.43) and gas (1.84) > chloroform (2.42) > methanol (2.69) > DMSO

(2.71), respectively. Additionally, the order of μ (in D) of the compounds was determined as FTA < ThTA < PhTA < NapTA < BFTA in gas and FTA < PhTA < NapTA < ThTA < BFTA in the other simulation media. However, the polarizability (in au) order of the compounds was determined as follows: FTA < ThTA < PhTA < BFTA < NapTA in all simulation media. Accordingly, the NapTA could be more polarizable than the other compounds and *vice versa* for FTA.

Moreover, the solvent effect on the ΔE, ΔH, and ΔG (au) quantities of the compounds was calculated, as presented in Table 6. Accordingly, each solvent environment provided stability for each compound relative to that of the gas phase counterpart. The $\Delta G_{sol.}$/(kJ mol^{-1}) order of the compounds was determined as BFTA (22.44) > FTA (22.05) > NapTA (21.95) > ThTA (19.36) > PhTA (18.35) in chloroform, and the orders of the methanol and DMSO media were the same as this trend. Similarly, the calculated $\Delta H_{sol.}$ and $\Delta E_{sol.}$ values disclosed the order of BFTA > FTA > NapTA > ThTA > PhTA in all simulation media. These values implied that the BFTA and then FTA compounds exhibited the highest stability among the compounds and *vice versa* for the PhTA compound in all simulation media.

3.3. Lipophilicity and water solubility features

In drug-design research, the lipophilicity and solubility in water are two key physicochemical parameters, and their predictions using computational tools play a critical role in the evaluation of which structure can be proper or not for usage in the related research field.

From Table 7, the averaged log $P_{o/w}$ values of the compounds changed in the following order: NapTA (3.09) > PhTA (2.13) > ThTA (2.10) > BFTA (2.03) > FTA (1.48); NapTA exhibited a more lipophilic feature among the compounds, and *vice versa* for FTA. However, the iLOGP approach revealed the log P_o/w order as NapTA (2.15) > BFTA (2.02) > FTA (1.74) > PhTA (1.69) > ThTA (1.66). Accordingly, all compounds could have the potential for oral bioavailability based on the iLOGP approach because the calculated lipophilicity values changed in the optimal range of −0.7 to +5.0.[56,57] Moreover, the XLOGP3 and WLOGP approaches showed the log $P_{o/w}$ values of the compounds ordered in the orders of NapTA > PhTA > ThTA > BFTA > FTA and NapTA > ThTA > PhTA > BFTA > FTA, respectively. According to the MLOGP method, the lipophilicity order was determined as NapTA (2.27) > PhTA (1.32) > BFTA (1.04) > ThTA (0.72) > FTA (−0.16); all compounds could be orally active because their calculated indices were lower than 4.15.[85] Although the calculated lipophilicity indices showed slightly different rankings, they all indicated that NapTA exhibited the most lipophilic behavior. Moreover, the FTA compound is slightly lipophilic among the compounds according to all approaches, except for the iLOGP approach.

In terms of pharmacokinetic features, the balance between lipophilicity and water solubility plays an essential role in the drug's effectiveness. The ESOL method revealed that the log S values of the compounds gave the order of FTA > BFTA > ThTA > PhTA > NapTA, while Ali's method gave the log S values that changed in the order of BFTA > FTA > PhTA > ThTA > NapTA. Additionally, the SILICO-IT approach presented the log S order of FTA > ThTA > PhTA > BFTA > NapTA. Herein, NapTA was determined to be slightly soluble in water according to all methods, as could be expected from the results of the lipophilicity index. In addition, the BFTA and FTA compounds, which include benzofuran and furan rings, respectively, are more soluble in water. As is well known, the solubility feature of a related system is classified by the quantity of the log S parameter as follows: insoluble < −10 < poorly −6 < moderately < −4 < soluble < −2 < very < 0 < highly.[56] Except for NapTA, all compounds were soluble in water because the calculated indexes of the compounds were located within the solubility limits.

Table 7 Lipophilicity and water solubility

Lipophilicity	PhTA	BFTA	FTA	ThTA	NapTA
log $P_{o/w}$ (iLOGP)	1.69	2.02	1.74	1.66	2.15
log $P_{o/w}$ (XLOGP3)	2.27	1.49	1.37	1.98	3.52
log $P_{o/w}$ (WLOGP)	2.40	2.13	1.99	2.46	3.55
log $P_{o/w}$ (MLOGP)	1.32	1.04	−0.16	0.72	2.27
log $P_{o/w}$ (SILICOS-IT)	2.98	3.46	2.45	3.70	3.95
Consensus log $P_{o/w}$	2.13	2.03	1.48	2.10	3.09
Water solubility					
log S (ESOL)	−2.98	−2.61	−2.34	−2.82	−4.09
Sol. (mg mL^{-1}) × 10^{-2}	18.7	53.7	75.9	27.3	1.85
Class	S	S	S	S	MS
log S (Ali)	−3.32	−2.70	−2.66	−3.61	−4.61
Sol. (mg mL^{-1}) × 10^{-2}	8.50	43.4	36.4	4.48	0.550
Class	S	S	S	S	MS
log S (SILICOS-IT)	−3.45	−3.75	−2.66	−2.72	−5.13
Sol. (mg mL^{-1}) × 10^{-2}	6.27	3.87	36.5	34.7	0.166
Class[a]	S	S	S	S	MS

[a] The abbreviations are defined as follows: S, soluble and MS, moderately soluble.

3.4. Pharmacokinetics and druglikeness studies

Herein, the pharmacokinetics and bioavailability parameters of the compounds are illustrated in Tables 8 and 9, respectively. Additionally, the BOILED-Egg "Brain Or IntestinaL EstimateD permeation" model and radar graphs, which were obtained from the SwissADME[56] and ADMETLab3 (ref. 86) tools, are illustrated in Fig. 4, respectively.

Table 8 Pharmacokinetics of the studied compounds

	PhTA	BFTA	FTA	ThTA	NapTA
GI absorption	High	High	High	High	High
BBB permeant	Yes	Yes	No	No	Yes
P-gp substrate	No	Yes	No	No	Yes
CYP1A2 inhibitor	Yes	Yes	Yes	Yes	Yes
CYP2C19 inhibitor	No	Yes	No	No	Yes
CYP2C9 inhibitor	No	No	No	No	No
CYP2D6 inhibitor	No	No	No	No	No
CYP3A4 inhibitor	No	Yes	No	No	Yes
log K_p (skin permeation)/cm s^{-1}	−5.76	−6.57	−6.34	−6.01	−5.18

Table 9 Drug-likeness and bioavailability values of the compounds

	PhTA	BFTA	FTA	ThTA	NapTA
Lipinski	Yes	Yes	Yes	Yes	Yes
Ghose	Yes	Yes	No; atoms < 20	No; atoms < 20	Yes
Veber	Yes	Yes	Yes	Yes	Yes
Egan	Yes	Yes	Yes	Yes	Yes
Muegge	No; MW < 200	Yes	No; MW < 200	No; MW < 200	Yes
Bioavail.	0.55	0.55	0.55	0.55	0.55

Accordingly, the GI absorption potency of all compounds was determined to be high, and all compounds were located in the white region of the BOILED-Egg (Fig. 4). In a previous study, it was reported by Daina and Zoete[87] that PSA lower than 142 Å^2 and log *P* between −2.3 and +6.8 provided a good HIA. Herein, the TPSA and consensus log *P* values of the compounds were predicted in the ranges of 67.15–95.39 Å^2 (see Table 1) and 1.48–3.09 (see Table 7), which confirmed the good GI absorption of the compounds.

The compounds PhTA, BFTA, and NapTA permeated through the BBB (blood–brain-barrier) passively, while FTA and ThTA compounds had no potency in terms of BBB-penetration. From Fig. 4, PhTA, BFTA, and NapTA appeared in the yolk region of the BOILED-Egg, but FTA and ThTA compounds were not placed in the yolk region. Additionally, the compounds BFTA and NapTA would be predicted to be effluated from the CNS by the glycoprotein since they appeared as blue dots in the BOILED-Egg model. On the other hand, the PhTA, FTA, and ThTA compounds appeared around the red dots, implying that these compounds were effluated from the CNS by the glycoprotein. Furthermore, all compounds could have inhibitory potency for the CYP1A2 gene. In terms of the cytochrome P450 enzyme, none of the compounds had potency for CYP2C9 and CYP2D6 inhibition. From Table 8, BFTA and NapTA compounds had inhibitory potency for CYP2C19 and CYP3A4 enzymes, while the other compounds did not. Herein, the log K_p (skin permeation) values of the compounds were predicted to be between −5.18 and −6.57 cm s^{-1}; the BFTA had slight skin

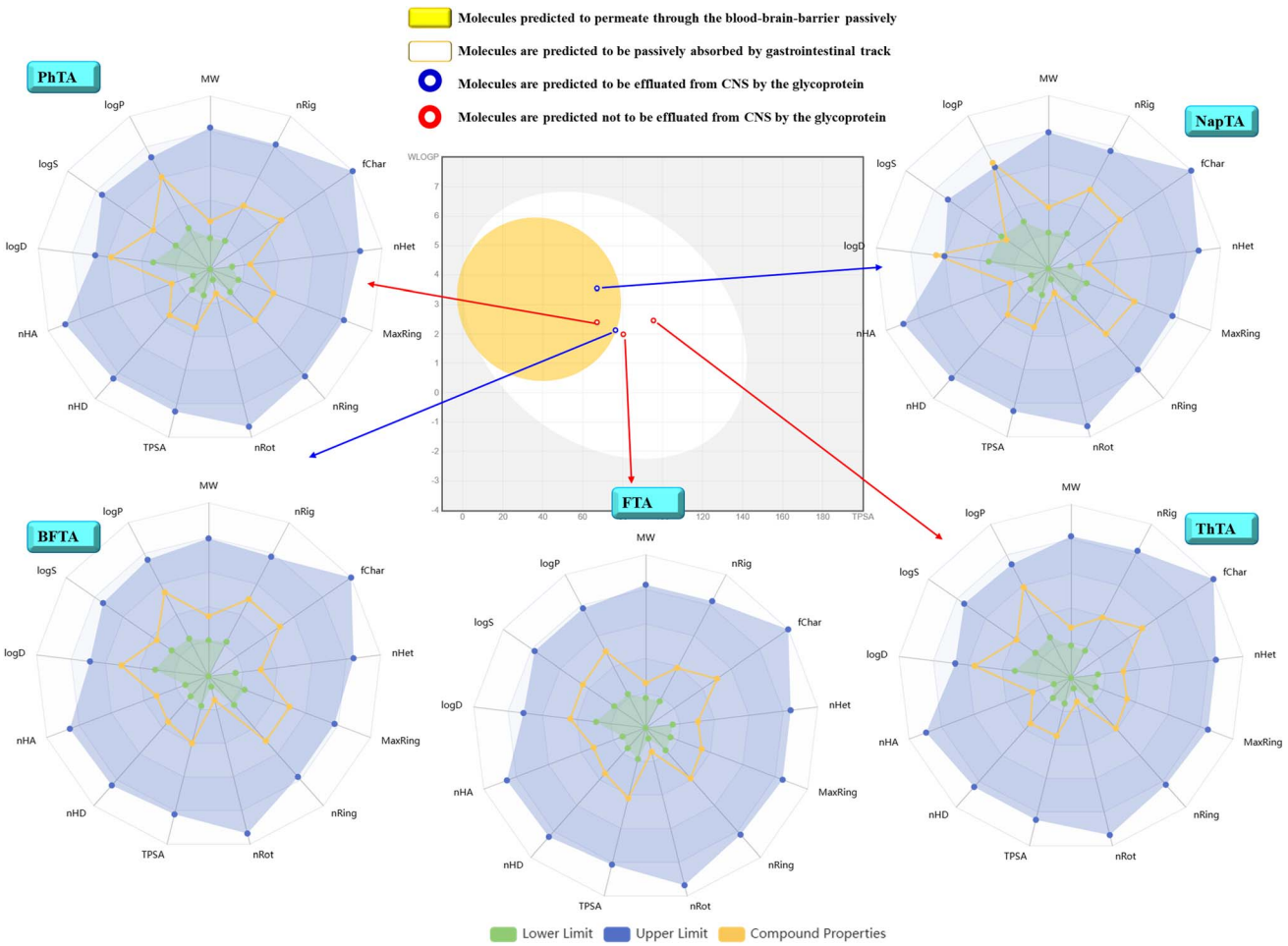

Fig. 4 BOILED-Egg and radar graphs.

permeability among the compounds, and the NapTA compound had more skin permeation. In previous studies, the log K_p (skin permeation) for famotidine and cortisone was reported at −7.63 cm s^{-1} and −7.29 cm s^{-1}, respectively;[88] all compounds studied in this work could have more skin penetration capability than those of famotidine and cortisone. Except for NapTA, the physicochemical properties of all compounds met the bioavailability criteria due to the yellow line appearing between the lower (green) and upper (blue) limits. However, the log *S* of the NapTA was out of the lower limit; besides, the log *P* and log *D* quantities were out of the upper bioavailability limit.

Moreover, Table 9 shows the drug-likeness and bioavailability scores of the compounds. Accordingly, the Lipinski, Veber, and Egan rules indicate that all compounds could meet bioavailability criteria. However, the Ghose method revealed that the atom numbers of the FTA and ThTA compounds were lower than 20 and had one violation of oral bioavailability. Except for NapTA, none of the compounds met the bioavailability criteria because the molecular weights of all compounds were lower than 200 g mol^{-1}. The bioavailability scores of all compounds were predicted to be 0.55, as expected from the Lipinski rules.

3.5. FMO (Frontier molecular orbital) analysis and MEP (molecular electrostatic potential)

In computational research, the FMO analysis's results have provided molecular insight into the prediction and evaluation of the possible chemical reactivity trend and active site of the relevant systems. For a long time, this computational approach has been applied to various kinds of molecular systems.[89,90] Herein, the calculated parameters of the compounds are presented in Table 10 in four simulation media.

In the gas phase, the reactivity parameters exhibited the following orders:

HOMO (eV): FTA (−5.588) > ThTA (−5.605) > NapTA (−5.663) > PhTA (−5.770) > BFTA (−5.794), LUMO (eV): FTA (−1.068) > PhTA (−1.186) > BFTA (−1.267) > ThTA (−1.298) > NapTA (−1.555), Δ*E* (eV): PhTA (4.584) > BFTA (4.527) > FTA (4.520) > ThTA (4.307) > NapTA (4.108), χ (eV): FTA (−3.328) > ThTA (−3.451) > PhTA (−3.478) > BFTA (−3.531) > NapTA (−3.609), η (eV): PhTA (2.292) > BFTA (2.264) > FTA (2.260) > ThTA (2.154) > NapTA (2.054), ω (eV): NapTA (0.117) > ThTA (0.102) > BFTA (0.101) > PhTA (0.097) > FTA (0.090), ω^+ (au): NapTA (0.060)> ThTA (0.048) > BFTA (0.047) > PhTA (0.044) > FTA (0.039), ω^- (au): NapTA (0.192) > BFTA (0.176) > ThTA (0.175) > PhTA (0.171) > FTA (0.162), ΔN_{max} (eV): NapTA (1.757) > ThTA (1.603) > BFTA (1.560) > PhTA (1.518) > FTA (1.472), $\Delta E_{back\text{-}donat}$ (eV): NapTA (−0.513) > ThTA (−0.538) > FTA (−0.565) > BFTA (−0.566) > PhTA (−0.573).

From Table 10, the PhTA compound preferred the intermolecular interactions more than the intramolecular charge transfer because the energy gap value was determined to be the highest in all simulation media, and *vice versa* for FTA. Moreover, the η, ω, ω^+, ΔN_{max}, and $\Delta E_{back\text{-}donat}$ values of the compounds exhibited the same order in all solvents. However, the electronic chemical potential values (χ, eV) of the compounds were predicted as follows: χ (eV): FTA (−3.403) >

Table 10 Chemical reactivity parameters

	Gas					Chloroform				
	PhTA	BFTA	FTA	ThTA	NapTA	PhTA	BFTA	FTA	ThTA	NapTA
H (−I) (eV)	−5.770	−5.794	−5.588	−5.605	−5.663	−5.821	−5.804	−5.637	−5.670	−5.721
L (−A) (eV)	−1.186	−1.267	−1.068	−1.298	−1.555	−1.276	−1.302	−1.170	−1.395	−1.666
Δ*E* (eV)	4.584	4.527	4.520	4.307	4.108	4.545	4.502	4.468	4.275	4.055
χ (eV)	−3.478	−3.531	−3.328	−3.451	−3.609	−3.548	−3.553	−3.403	−3.532	−3.693
η (eV)	2.292	2.264	2.260	2.154	2.054	2.272	2.251	2.234	2.138	2.027
ω (eV)	0.097	0.101	0.090	0.102	0.117	0.102	0.103	0.095	0.107	0.124
ω^+ (au)	0.044	0.047	0.039	0.048	0.060	0.047	0.048	0.043	0.052	0.065
ω^- (au)	0.171	0.176	0.162	0.175	0.192	0.177	0.179	0.168	0.182	0.201
ΔN_{max} (eV)	1.518	1.560	1.472	1.603	1.757	1.562	1.578	1.524	1.653	1.822
$\Delta\varepsilon_{back\text{-}donat.}$ (eV)	−0.573	−0.566	−0.565	−0.538	−0.513	−0.568	−0.563	−0.558	−0.534	−0.507
	Methanol					DMSO				
	PhTA	BFTA	FTA	ThTA	NapTA	PhTA	BFTA	FTA	ThTA	NapTA
H (−I) (eV)	−5.859	−5.828	−5.677	−5.712	−5.764	−5.862	−5.830	−5.680	−5.714	−5.767
L (−A) (eV)	−1.326	−1.332	−1.221	−1.451	−1.723	−1.329	−1.334	−1.225	−1.455	−1.727
Δ*E* (eV)	4.533	4.496	4.456	4.260	4.041	4.533	4.496	4.455	4.259	4.040
χ (eV)	−3.592	−3.580	−3.449	−3.582	−3.743	−3.595	−3.582	−3.452	−3.585	−3.747
η (eV)	2.267	2.248	2.228	2.130	2.021	2.266	2.248	2.227	2.130	2.020
ω (eV)	0.105	0.105	0.098	0.111	0.127	0.105	0.105	0.098	0.111	0.128
ω^+ (au)	0.049	0.049	0.045	0.055	0.068	0.049	0.049	0.045	0.055	0.068
ω^- (au)	0.181	0.181	0.172	0.186	0.205	0.181	0.181	0.172	0.187	0.206
ΔN_{max} (eV)	1.585	1.593	1.548	1.681	1.853	1.586	1.594	1.550	1.683	1.855
$\Delta\varepsilon_{back\text{-}donat.}$ (eV)	−0.567	−0.562	−0.557	−0.533	−0.505	−0.567	−0.562	−0.557	−0.532	−0.505

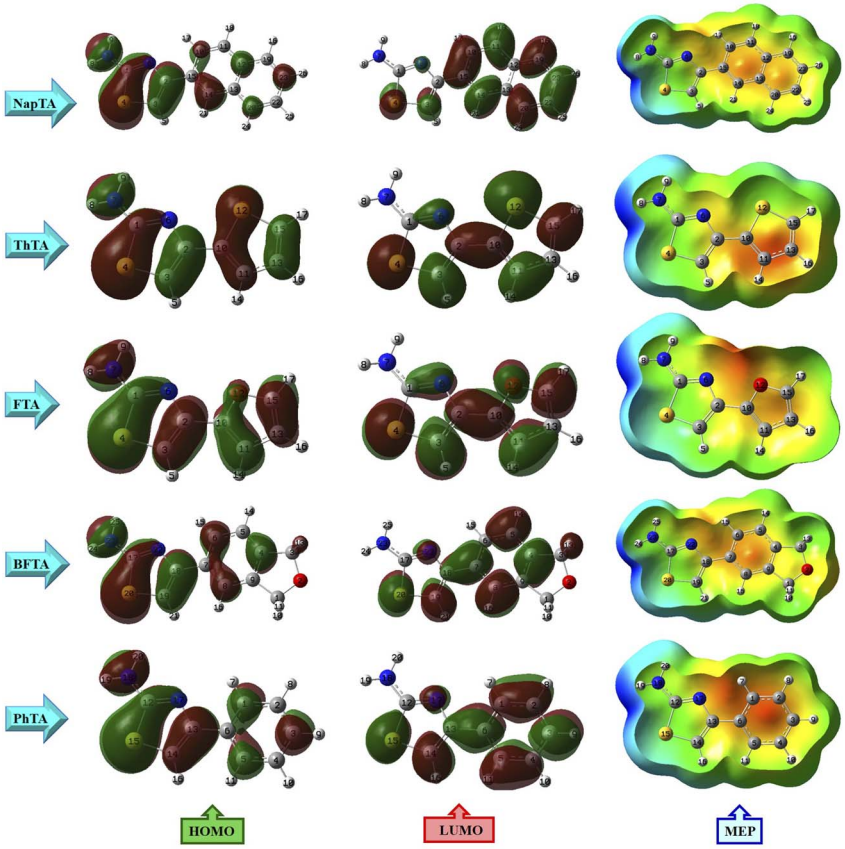

Fig. 5 HOMO and LUMO (isoval: 0.02) and MEP (isoval: 0.0004) plots.

ThTA (−3.532) > PhTA (−3.548) > BFTA (−3.553) > NapTA (−3.693) in gas, whereas χ order was determined in the order of FTA (−3.449) > BFTA (−3.580) > ThTA (−3.582) > PhTA (−3.592) > NapTA (−3.743) in chloroform. A similar order of the electronic chemical potential was estimated for the methanol and DMSO phases. Herein, the FTA could be less electronically stable among the compounds, and NapTA is the most stable electronically. Related to the electronic chemical potential, the differences between the gas phase and the other phases were that the BFTA compound was more stable than the PhTA and then the ThTA compounds, while the PhTA could be more stable than the ThTA and then the BFTA compounds. Accordingly, the results revealed that the PhTA compound was determined to be the hardest compound among the compounds, while NapTA was the softest. Furthermore, NapTA was the most electrophilic compound, while the FTA could be the least electrophilic compound. From Table 10, the NapTA compound had the highest charge transfer capability, while the FTA had the least charge transfer capability. Additionally, the PhTA compound gained the most stability *via* back-donation, among the compounds, and NapTA gained the least stability *via* back-donation, with the orders of NapTA (−0.507) > ThTA (−0.534) > FTA (−0.558) > BFTA (−0.563) > PhTA (−0.568) in gas and the orders of NapTA (−0.505) > ThTA (−0.532) > FTA (−0.557) > BFTA (−0.562) > PhTA (−0.567) in DMSO.

Moreover, the FMO densities and MEP plots showed the possible reactive sites and electron-rich and electron-poor regions for the electrophilic and nucleophilic attack reactions. Herein, Fig. 5 shows the FMO amplitudes and MEP plots of the compounds. In fact, the LUMO for all compounds expanded on the whole surface except for the $-NH_2$ group, while the HOMO exhibited different types of expansion on the related surfaces of the compounds. For instance, the HOMO for FTA and ThTA compounds was expanded on the whole molecular surface, while the LUMO, the HOMO for the BFTA compound was separated on the molecular surface except for the dihydrofuran unit, while the LUMO was delocalized on the whole surface except for the –O–C– atoms of the dihydrofuran unit. MO was separated on the molecular surface except for the $-NH_2$ group. Additionally, the HOMO of PhTA was separated on the whole thiazol-2-amine ring and benzene ring by more than half. The HOMO of the NapTA compound appeared on the mostly thiazol-2-amine ring and half on the naphthalene unit of the compound, while the LUMO of this compound was mostly observed on the naphthalene unit and the thiazol-2-amine ring half. As is well known, the HOMO is related to the possible sites for nucleophilic attacks, and the LUMO is associated with electrophilic attack sites. Accordingly, the $-NH_2$ group was not related to the electrophilic attack reactions due to the lack of LUMO density in this group. Moreover, the MEP plot of the PhTA compound implied that the Hs of the $-NH_2$ group would be a possible site for the nucleophiles because of these atoms bearing blue color (V > 0) as an indicator of the electron-poor region as a function of the electrostatic potential on the

surface. Additionally, the red color ($V < 0$) for the PhTA compound appeared on the aromatic benzene ring, which was the electron-rich region. Furthermore, the $-NH_2$ group for the BFTA and FTA compounds would be a suitable region for the nucleophiles, while the O atom around, which was covered by red color, could be the proper site for the electrophiles. The color scheme of the MEP plots has provided a molecular insight into the possible active sites of the related molecules.

3.6. Molecular docking analysis

Molecular docking is one of the most useful computational tools for predicting the binding modes and orientation of a molecule against a target biomacromolecule. In drug discovery research, the method can identify and optimize drug candidates and gain insight into the detailed structure of the protein–ligand complex, which generally is not available experimentally.[91] In addition, molecular docking helps estimate how structural modifications in small molecules influence their pharmaceutical properties. Thus, this approach both accelerates drug discovery and provides valuable insights into the molecular interactions underlying various biological processes.[92]

Angiogenesis refers to "the formation of new blood vessels from pre-existing ones". Physiological angiogenesis occurs predominantly during growth until adolescence and proceeds at a much slower rate in adults, where it plays roles in processes such as wound healing and pregnancy. Additionally, under conditions such as inflammation, diabetic retinopathy, atherosclerosis, and tumor development, pathological angiogenesis arises. A major regulator of this process is vascular endothelial growth factor (VEGF).[93] The VEGF family consists of seven glycoproteins that exert biological activity by binding to specific transmembrane tyrosine kinase receptors, namely VEGFR-1, VEGFR-2, VEGFR-3, and neuropilins (NP-1 and NP-2). Among these, VEGFR-2 is of particular importance due to its key role in endothelial cell proliferation and migration. Consequently, VEGFR-2 represents a crucial therapeutic target for suppressing angiogenesis in cancer and other diseases. Several VEGFR-2 inhibitors have already been incorporated into cancer treatment strategies,[94] and research on the development of novel inhibitors is actively ongoing. For instance, Al-Hazmy *et al.* investigated coumarin derivatives for their antiproliferative potential through molecular docking studies against the VEGFR-2 crystal structure. Their analysis revealed hydrogen bonding interactions with Asn921 and Cys917, along with π-interactions involving Val914 and Leu1038.[95] Similarly, a benzimidazole-type N-heterocyclic carbene (NHC) and its silver complex were studied owing to their anticancer properties with both experimental and theoretical methods by Serdaroğlu *et al.* docking studies against VEGFR-2 showed that the silver complex exhibited stronger binding affinity (-7.59 kcal mol^{-1}) than its precursor salt, with key interactions with Asp1044, Glu883, Ile886, Val896, Cys1022, and His1024.[96] In another study, Pinki and Chaudhary analyzed novel macrocyclic Zn(II) complexes for their anticancer activity against breast and colon cancer cells. Their additional docking analyses using VEGFR-2 revealed hydrogen bonding with Lys866 in addition to hydrophobic interactions with Leu838, Cys917, Arg1030, and

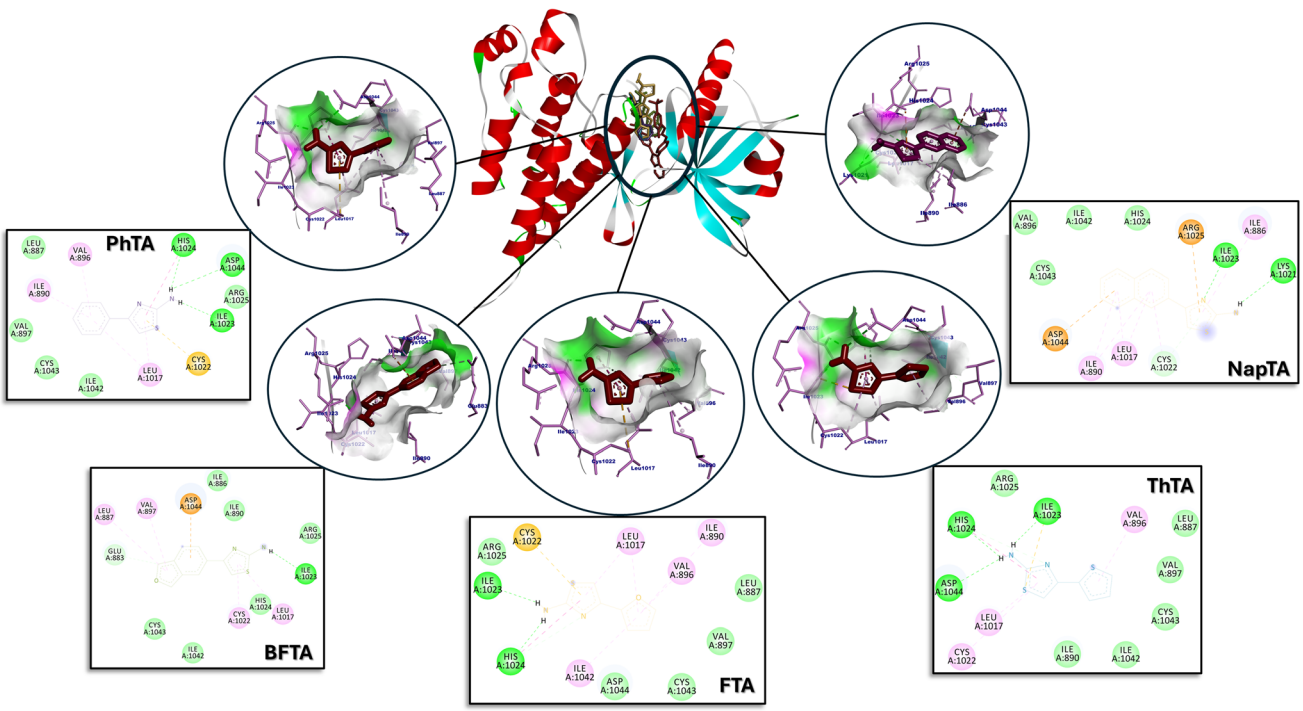

Fig. 6 Interaction residues and the interaction types of the molecules against the VEGFR-2 crystal structure (in 2D illustration, dark green and pale green: H-bond, pink: alkyl interactions, yellow: pi-sulfur interactions, green: van der Waals interactions, fuchsia: pi-amide stacked, purple: pi-sigma, and orange: pi-anion/cation).

Asp1044.[97] In this study, molecular docking analysis was conducted to elucidate the potential mechanisms responsible for the anticancer activity of the synthesized compounds through their interactions with VEGFR-2. All compounds were found to bind within the same active site region of the target protein, displaying only minor differences in orientation. The interacting amino acid residues were largely consistent with those identified for the reference ligand, 4-amino-furo[2,3-*d*]pyrimidine (AAFP), and they agreed with previously reported findings. AAFP, employed as a positive control, exhibited a binding energy of −5.61 kcal mol^{-1} and formed hydrogen bonds with Glu883, Glu915, Cys917, and Asp1044. The root mean square deviation (RMSD) values of the predicted binding poses were ≤2 Å, supporting the reliability and accuracy of the docking results. The best binding constant was determined for NapTA as −5.74 kcal mol^{-1}. H-bonds with Lys1021, Cys1022, and Ile1023, pi-interactions with Arg1025 and Asp1044, and alkyl interactions with Ile886, Ile890, and Leu1017 were determined in addition to van der Waals interactions with Val896, His1024, Ile1042, and Cys1043. PhTA, BFTA, FTA, and ThTA had binding affinities of −5.23, −5.52, −5.00, and −5.12 kcal mol^{-1}, respectively. H-bonds were recorded for all molecules: three H-bonds with Ile1023, His1024, and Asp1044 for PhTA; one H-bond with Glu883 for BFTA; two H-bonds with Ile1023 and His1024 for FTA; and three H-bonds with Ile1023, His1024, and Asp1044 for ThTA. All the interaction details are depicted in Fig. 6.

Estrogen receptors (ERs) are specialized proteins for the mediation of the physiological effects of estrogen hormones and are members of the nuclear receptor superfamily. By binding to these receptors, estrogens regulate the maintenance and differentiation of nervous, reproductive, and skeletal tissues. Importantly, estrogen receptors can be expressed in many breast cancer tumors, and their growth is stimulated by estrogen. Consequently, modulation of ER activity represents a key therapeutic strategy in the treatment of breast cancer. Similar receptor-targeted approaches are also applied in the management of osteoporosis and certain cardiovascular diseases.[98] Several molecular docking studies have explored novel ligands for ER modulation. For example, Kumar *et al.* synthesized new quinoline derivatives with potential anticancer activity and evaluated their interactions with estrogen receptors. The docking scores ranged from −8.04 to −9.39 kcal mol^{-1}, with hydrogen bonding interactions identified at residues Thr347, Glu353, and Arg394.[99] Similarly, Sarkar and Maiti investigated the organosulfur and flavonoid components of garlic as potential ER-targeting agents. Among the flavonoids, kaempferol exhibited the most favorable binding affinity, with a score of −8.0 kcal mol^{-1}.[100] In a more recent study, several chlorogenic acid derivatives were examined by Sehrawat *et al.* using silico approaches. The most active ligand presented a hydrogen bond with Asp351, π-interactions with Tyr526, and hydrophobic interactions, highlighting its potential as a therapeutic candidate.[101] In this study, a molecular docking analysis was performed against the human estrogen receptor. All compounds were found to bind within the same active site region of the target protein, displaying only minor differences in orientation. The interacting amino acid residues were largely

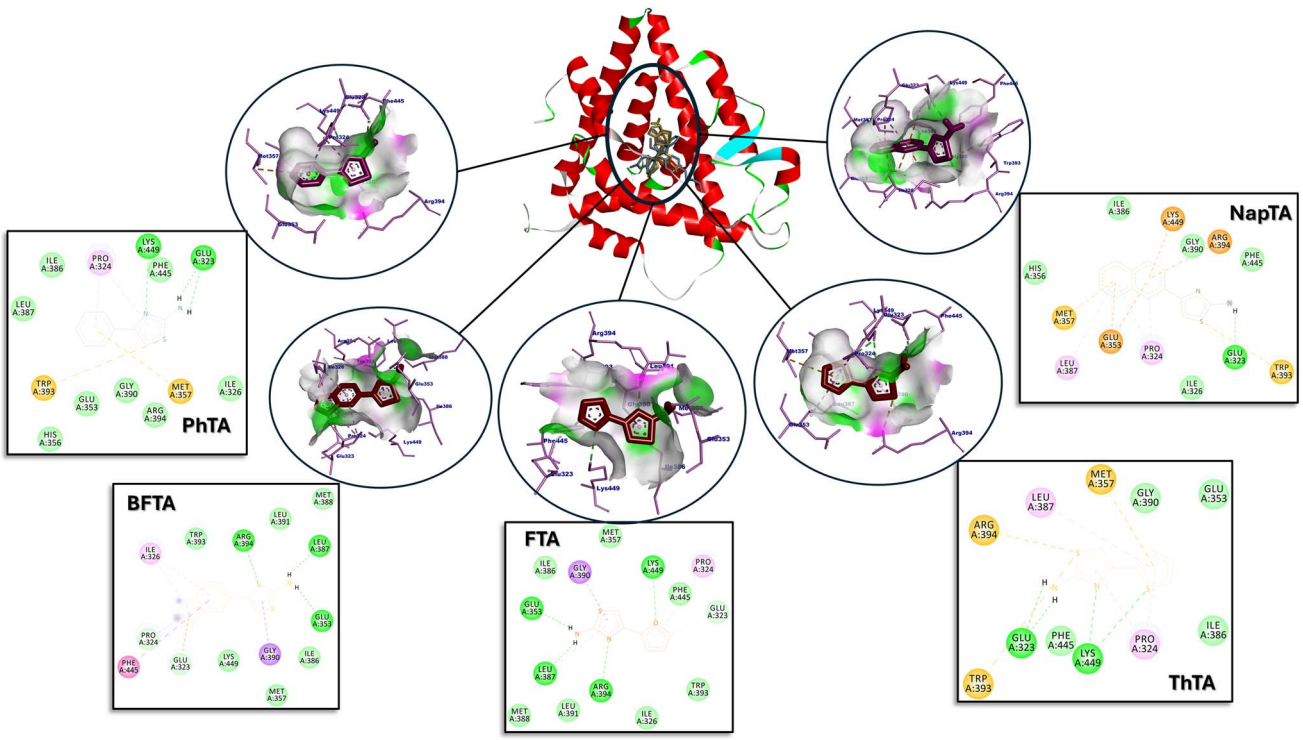

Fig. 7 Interaction residues and the interaction types of the molecules against the estrogen receptor crystal structure (in 2D illustration, dark green and pale green: H-bond, pink: alkyl interactions, yellow: pi-sulfur interactions, green: van der Waals interactions, fuchsia: pi-amide stacked, and purple: pi-sigma).

consistent with those identified for the reference ligand, hydroxytamoxifen, and they agreed with previously reported findings. AAFP, employed as a positive control, exhibited a binding energy of −10.35 kcal mol^{-1} and formed hydrogen bonds with Asp351, Glu353, and Arg394. The root mean square deviation (RMSD) values of the predicted binding poses were ≤2 Å, supporting the reliability and accuracy of the docking results. The best binding constant was determined for NapTA as −6.58 kcal mol^{-1}. H-bond with Glu323; pi-interactions with Glu353, Met357, Trp393, Arg394, and Lys449; and alkyl interactions with Pro324 and Leu387 were determined in addition to van der Waals interactions with Ile326, His356, Ile386, Gly390, and Phe445. PhTA, BFTA, FTA, and ThTA had binding affinities of −5.53, −5.97, −5.09, and −5.09 kcal mol^{-1}, respectively. H-bonds were recorded for all molecules: one H-bond with Lys449 for PhTA; five H-bonds with Glu323, Pro324, Glu353, Leu387, and Arg394 for BFTA; five H-bonds with Glu323, Glu353, Leu387, Arg394, and Lys449 for FTA; and two H-bonds with Glu323 and Lys449 for ThTA. All the interaction details are presented in Fig. 7.

Cytochrome P450 (CYPs) constitutes a large enzyme superfamily responsible for the metabolism of various xenobiotics, such as drugs, industrial chemicals, and pesticides. In addition to these external compounds, several endogenous molecules such as prostaglandins, steroids, and fatty acids also serve as physiological substrates for CYP enzymes.[102] Alterations in the expression levels of CYPs, often resulting from gene polymorphisms or structural variations, can significantly influence xenobiotic metabolism, thereby affecting tolerance to these compounds. Among the CYP family, P450 17α-hydroxylase plays a critical role in androgen biosynthesis in humans, making it an important therapeutic target in the treatment of ovarian, colorectal, breast, and prostate cancers.[103] Several molecular docking studies have been conducted to identify potential CYP inhibitors with anticancer properties. For instance, Dhawale *et al.* evaluated the interactions of various phytoconstituents with CYP450 and reported strong binding affinities for peonidin, pelargonidin, malvidin, and berberine, with the best affinity recorded at −7.574 kcal mol^{-1} through notable hydrogen bonding interactions.[104] Similarly, Bahzad *et al.* investigated novel Cu(II) complexes with mixed ligands for anticancer potential. Molecular docking against CYP450 revealed binding affinities ranging from −5.60 to −7.91 kcal mol^{-1}.[105] In another study, Tajiani *et al.* performed molecular docking of natural flavanols against the CYP450 crystal structure in a PC-3 cell line model. Abiraterone displayed the most favorable binding profile, with an affinity of −10.3 kcal mol^{-1}, forming interactions with residues Val483, Glu305, Arg239, and Cys442.[106] In this study, the aminothiazole-type molecules were analyzed to reveal their interactions with human cytochrome P450 using molecular docking methods. All molecules interacted with the same area of the target crystal, which is in accordance with abiraterone (the reference molecule). The root mean square deviation (RMSD) values of the predicted binding poses were ≤2 Å, supporting the reliability and accuracy of the docking results. The best binding constant

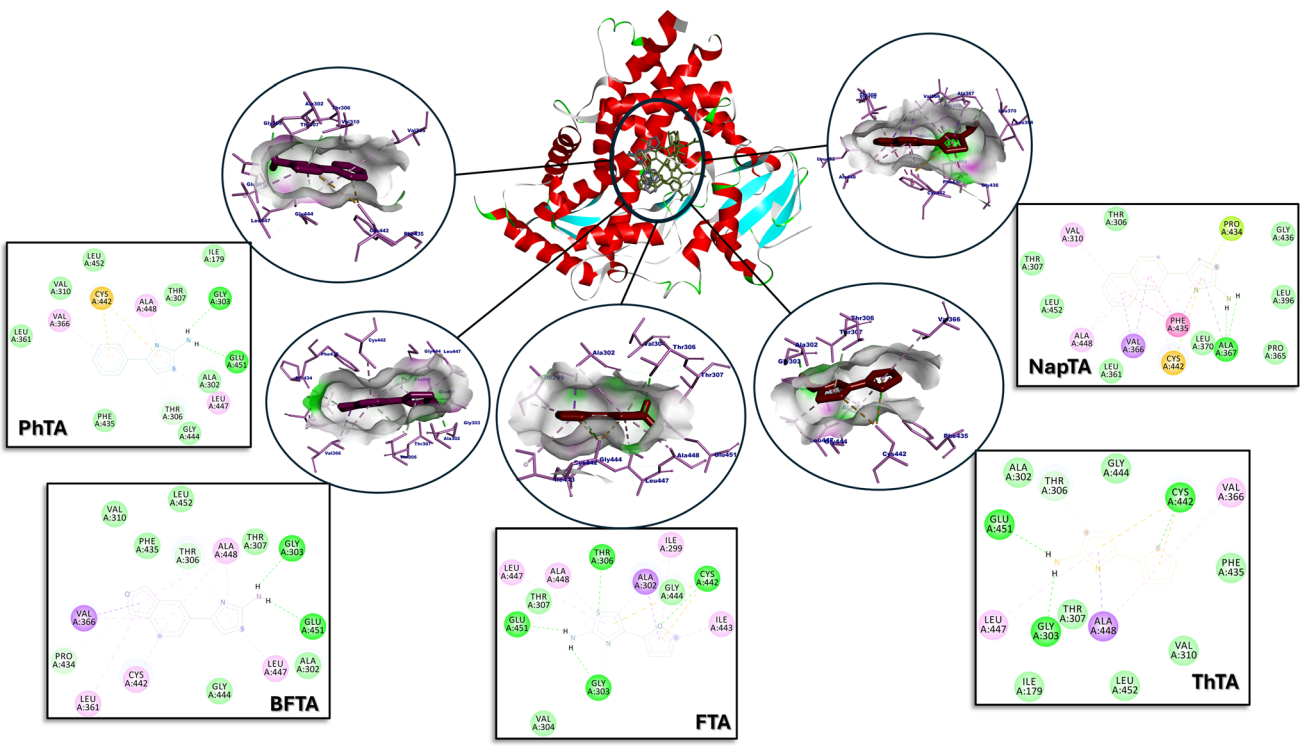

Fig. 8 Interaction residues and the interaction types of the molecules against the cytochrome P450 crystal structure (in 2D illustration, dark green and pale green: H-bond, pink: alkyl interactions, yellow: pi-sulfur interactions, green: van der Waals interactions, fuchsia: pi-amide stacked, grass green: pi-lone pair, and purple: pi-sigma).

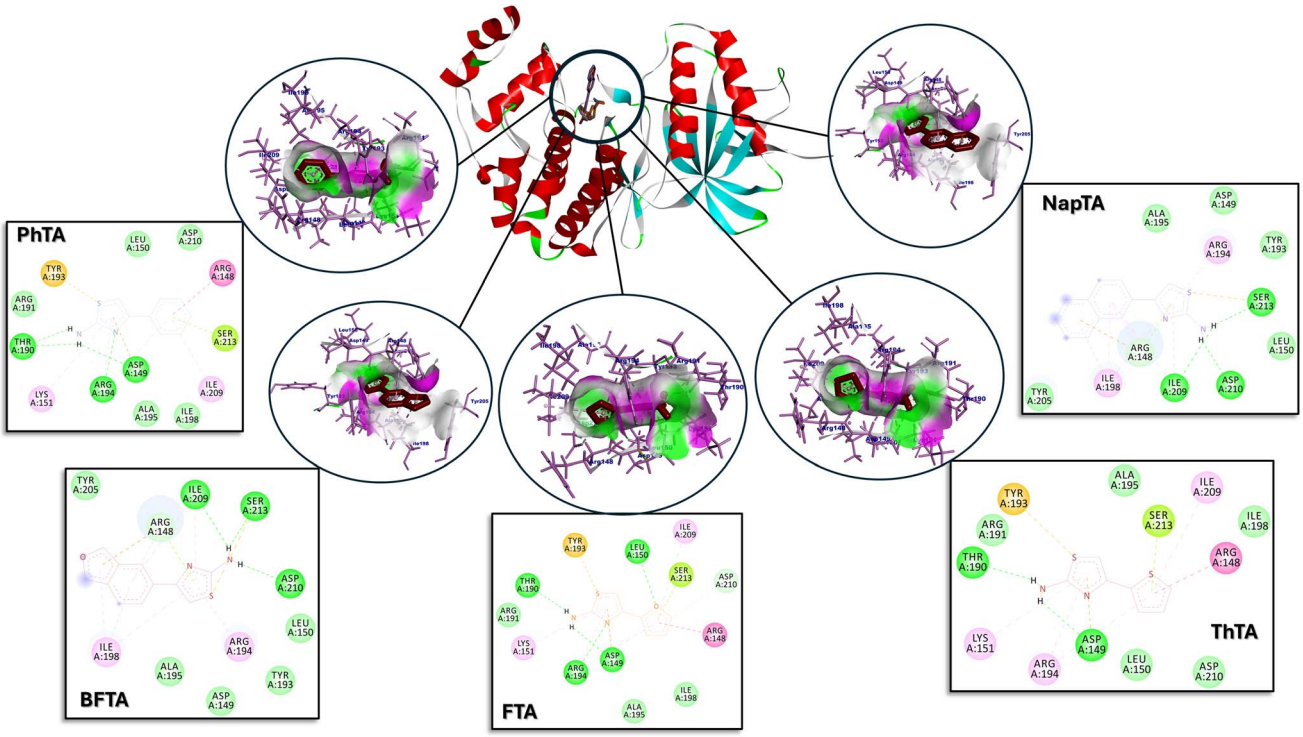

Fig. 9 Interaction residues and the interaction types of the molecules against the ERK2 crystal structure (in 2D illustration, dark green and pale green: H-bond, pink: alkyl interactions, yellow: pi-sulfur interactions, green: van der Waals interactions, fuchsia: pi-amide stacked, and grass green: pi-lone pair).

was determined for NapTA as −6.83 kcal mol^{-1}. H-bond with Ala367, pi-interactions with Val366, Pro434, Phe435, and Cys442, and alkylic interactions with Val310, and Ala448 were determined in addition to van der Waals interactions with Thr306, Leu361, Pro365, Leu370, Leu396, Gly436, and Leu452. PhTA, BFTA, FTA, and ThTA had the following binding affinities: −5.48, −6.24, −4.70, and −5.10 kcal mol^{-1}, respectively. H-bonds were recorded for all molecules: three H-bonds with Gly303, Thr306, and Glu451 for PhTA; four H-bonds with Gly303, Thr306, Pro434, and Glu451 for BFTA; four H-bonds with Gly303, Thr306, Cys442, and Glu451 for FTA; and four H-bonds with Gly303, Thr306, Cys442, and Glu451 for ThTA. All the interaction details are depicted in Fig. 8.

Mitogen-activated protein kinases (MAPKs) are a group of protein kinases that play an important role in signaling pathways for responding to extracellular stimuli, such as growth factors, hormones, and environmental stresses. Extracellular signal-regulated kinase 2 (ERK2) is one of the isoforms of this kinase family. ERK2 plays an important role in regulating cell proliferation, differentiation, and survival, as well as gene expression.[107] Dysregulation of the ERK signaling pathway is associated with various diseases, including cancer and neurodegenerative disorders. Small ERK2 inhibitors are considered recent potential anticancer drugs.[108] Zhao *et al.* investigated the inhibitory activities of 20(R, S)-PPT and confirmed their results using molecular docking methods against some target proteins, including ERK2.[109] Niu *et al.* discussed the binding mechanism of pyrrolidine piperidines using molecular docking techniques and provided valuable information for efficient Type I1/2 ERK2 inhibitors.[110] In this study, the aminothiazole-type molecules were analyzed to reveal their interactions with ERK2 by applying molecular docking methods. All molecules interacted with the same area of the target crystal, which is in accordance with SCH772984 (the reference molecule). The root mean square deviation (RMSD) values of the predicted binding poses were ≤2 Å, supporting the reliability and accuracy of the docking results. The best binding constant determined for PhTA was −6.08 kcal mol^{-1}. H-bonds with Asp149, Thr190, and Arg194, pi-interactions with Arg148, Tyr193, and Ser213, and alkylic interactions with Lys151 and Ile209 were determined in addition to van der Waals interactions with Leu150, Arg191, Ala195, Ile198, and Asp210. BFTA, FTA, ThTA, and NapTA had binding affinities of −5.22, −5.95, −6.03, and −5.16 kcal mol^{-1}, respectively. H-bonds were recorded for all molecules: four H-bonds with Arg148, Ile209, Asp210, and Ser213 for BFTA; five H-bonds with Asp149, Leu150, Thr190, Arg194, and Asp210 for FTA; two H-bonds with Asp149 and Thr190 for ThTA; and four H-bonds with Arg148, Ile209, Asp210, and Ser213 for NapTA. All the interaction details are illustrated in Fig. 9.

4. Conclusions

In conclusion, we have demonstrated a novel and efficient synthesis of 2-aminothiazole derivatives using iodine and molecular sieves derived from various ketones. This innovative approach aligns with ongoing efforts in green chemistry and emphasizes the importance of developing greener alternatives for sustainable chemical processes. The use of readily available

starting materials, high selectivity, and mild reaction conditions makes this method particularly attractive. Additionally, aminothiazole-type molecules were evaluated for their inhibition effect against VEGFR-2, estrogen receptor, cytochrome P450, and ERK2 using the molecular docking method. NapTA has the best binding affinity against VEGFR-2, estrogen receptor, and cytochrome P450 with −5.74, −6.58, and −6.83 kcal mol^{-1} binding affinity, respectively, while the strongest interactions were recorded between ERK2 and PhTA with a −6.08 kcal mol^{-1} binding constant. All the molecules had H-bonds against all target molecules, and the interaction residues were in accordance with the reference molecules. Accordingly, aminothiazole derivative molecules should be evaluated for these biomacromolecules. In future studies, new polycyclic substitutions should be a remarkable way to investigate possible inhibitor effects.

Author contributions

Goncagül Serdaroğlu: supervision, project administration, formal analysis, writing – review & editing. Nesimi Uludağ: validation, formal analysis, resources, writing – review & editing. Elvan Üstün: validation, formal analysis, resources, writing – review & editing.

Conflicts of interest

No conflicts of interest to be declared.

Data availability

Data are available in the manuscript and the supplementary information (SI). Supplementary information is available. See DOI: https://doi.org/10.1039/d5ra09930g.

Acknowledgements

Financial support for this research was received from the Scientific and Technological Research Council of Turkey (TUBITAK Project No. 112T503). The authors thank Namık Kemal University for the analysis of the structure of this article. All calculations have been carried out at the TUBITAK ULAKBIM, High Performance and Grid Computing Center (TR-Grid e-Infrastructure).

References

1 D. Das, P. Sikdar and M. Bairagi, Recent development of 2-aminothiazoles in medicinal chemistry, *Eur. J. Med. Chem.*, 2016, **109**, 89–98.
2 H. R. Maradiya and V. S. Patel, Synthesis and application of disperse dyes based on 2-aminothiazole derivatives, *Chem. Heterocycl. Compd.*, 2003, **39**, 357–363.
3 G. Turan-Zitouni, Z. A. Kaplancikli and A. Ozdemir, Synthesis and antituberculosis activity of some *N*-pyridyl-*N*′-thiazolylhydrazine derivatives, *Eur. J. Med. Chem.*, 2010, **45**, 2085–2088.
4 A. Cohen, P. Verhaeghe, M. D. Crozet, S. Hutter, P. Rathelot, P. Vanelle and N. Azas, Tandem synthesis and *in vitro* antiplasmodial evaluation of new naphtho[2,1-*d*]thiazole derivatives, *Eur. J. Med. Chem.*, 2012, **55**, 315–324.
5 T. D. Donohoe, M. A. Kabeshov, A. H. Rathi and I. E. D. Smith, Direct Preparation of Heteroaromatic Compounds from Alkenes, *Synlett*, 2010, **19**, 2956–2958.
6 J. S. Yadav, B. V. Subba Reddy, Y. Gopala Rao and A. V. Narsaiah, First example of the coupling of α-diazoketones with thiourea: a novel route for the synthesis of 2-aminothiazoles, *Tetrahedron Lett.*, 2008, **49**, 2381–2383.
7 G. Serdaroğlu, N. Uludag and E. Üstün, Green Synthesis of Pyrrole Derivatives Catalyzed by Molecular Sieves: DFT, ADMT, and Molecular Docking Investigations, *ChemistrySelect*, 2024, **9**, e202400019.
8 X. Y. Meng, H. X. Zhang, M. Mezei and M. Cui, Molecular docking: a powerful approach for structure-based drug discovery, *CCADD*, 2011, **7**(2), 146–157.
9 K. Aksu, M. Ç. Ayvaz, Ö. F. Çelik, G. Serdaroğlu, E. Üstün and L. Kelebekli, Synthesis, Biological Activities, DFT Calculations, and Molecular Docking Studies of O-Methyl-Inositols, *Chem. Biodiversity*, 2025, **22**(6), e202402346.
10 C. S. Abhinand, R. Raju, S. J. Soumya, P. S. Arya and P. R. Sudhakaran, VEGF-A/VEGFR2 signaling network in endothelial cells relevant to angiogenesis, *J. Cell Commun. Signaling*, 2016, **10**(4), 347–354.
11 H. Hua, H. Zhang, Q. Kong and Y. Jiang, Mechanisms for estrogen receptor expression in human cancer, *Exp. Hematol. Oncol.*, 2018, **7**(1), 24.
12 F. J. Gonzalez, Human cytochromes P450: problems and prospects, *TIPS*, 1992, **13**, 346–352.
13 L. Zhuang, C. S. Lee, R. A. Scolyer, S. W. McCarthy, A. A. Palmer, X. D. Zhang and P. Hersey, Activation of the extracellular signal regulated kinase (ERK) pathway in human melanoma, *J. Clin. Pathol.*, 2005, **58**(11), 1163–1169.
14 A. A. Tikhii, I. V. Zhikharev and V. D. Dyachenko, Optical Absorption Spectra of (E)-2-(2-Aryl-1-Cyanovinyl)-4-Cyclopropylthiazoles, *J. Appl. Spectrosc.*, 2025, **92**, 16–25.
15 A. Ö. Kesebir, Y. Demir, R. Sağlamtaş and A. Öztekin, Evaluation of 2-Aminothiazoles as α-Glucosidase Inhibitors: DFT, Molecular Docking, and Antioxidant Studies, *Biotechnol. Appl. Biochem.*, 2025, DOI: 10.1002/bab.70054.
16 A. V. Migulin, C. V. Milyutin, B. V. Lichitsky, S. M. Korobkov and A. N. Komogortsev, Investigation of the photochemical behavior of allomaltol-containing 2-aminothiazole derivatives, *Org. Biomol. Chem.*, 2025, **23**(17), 4172–4185.
17 D. Bumażnik and M. Sałdyka, UV-Induced Photodegradation of 2-Aminothiazole-4-Carboxylic Acid: Identification of New Carbodiimide Molecules, *Molecules*, 2025, **30**, 3713.
18 M. Gökalp, T. Tilki and Ç. K. Atay, Newly Synthesized Aminothiazole Based Disazo Dyes and Their Theoretical Calculations, *Polycyclic Aromat. Compd.*, 2023, **44**(2), 860–882.

19 M. Shaiwale, N. N. Som, P. K. Jha and A. Ballabh, A simple and efficient synthesis of a series of *N*-(thiazol-2-yl) piperidine-2, 6-dione compounds and their interesting NLO properties, *CrystEngComm*, 2024, **26**(23), 3069–3076.
20 M. A. Abdulridua, H. A. H. AL-Sa'idy and A. E. Al-Snafi, Synthesis, characterization, anticancer, and antioxidant studies of new azo-Schiff compounds derived from 2-naphthol, *Drug Discovery*, 2025, **19**, e3dd2037.
21 Y. Miyazaki, S. Matsunaga, J. Tang, Y. Maeda, M. Nakano, R. J. Philippe and R. T. Nolte, Novel 4-amino-furo [2,3-*d*] pyrimidines as Tie-2 and VEGFR2 dual inhibitors, *BMCL*, 2005, **15**(9), 2203–2207.
22 A. K. Shiau, D. Barstad, P. M. Loria, L. Cheng, P. J. Kushner, D. A. Agard and G. L. Greene, The structural basis of estrogen receptor/coactivator recognition and the antagonism of this interaction by tamoxifen, *Cell*, 1998, **95**(7), 927–937.
23 N. M. DeVore and E. E. Scott, Structures of cytochrome P450 17A1 with prostate cancer drugs abiraterone and TOK-001, *Nature*, 2012, **482**(7383), 116–119.
24 A. Chaikuad, E. Tacconi, J. Zimmer, Y. Liang, N. S. Gray, M. Tarsounas and S. Knapp, A unique inhibitor binding site in ERK1/2 is associated with slow binding kinetics, *Nat. Chem. Biol.*, 2014, **10**(10), 853–860.
25 R. Huey, G. M. Morris and S. Forli, Using AutoDock 4 and AutoDock Vina with AutoDockTools: a tutorial, *Scripps Res. Inst. Mol. Graphics. Lab.*, 2012, **10550**(92037), 1000.
26 G. M. Morris, R. Huey and A. J. Olson, Using AutoDock for ligand-receptor docking, *Curr. Protoc. Bioinf.*, 2008, **24**(1), 8–14.
27 N. S. Pagadala, K. Syed and J. Tuszynski, Software for molecular docking: a review, *Biophy. Rev.*, 2017, **9**(2), 91–102.
28 S. Hkiri, K. A. Coşkun, E. Üstün, A. Samarat, Y. Tutar, N. Şahin and D. Sémeril, Silver (I) complexes based on oxadiazole-functionalized α-aminophosphonate: Synthesis, structural study, and biological activities, *Molecules*, 2022, **27**(23), 8131.
29 G. M. Morris and M. Lim-Wilby, Molecular docking, in *Molecular Modeling of Proteins*, Totowa, NJ, Humana Press, 2008, pp. 365–382.
30 A. D. Becke, A new mixing of Hartree–Fock and local density-functional theories, *J. Chem. Phys.*, 1993, **98**, 1372–1377.
31 C. Lee, W. Yang and R. G. Parr, Development of the Colle-Salvetti correlation-energy formula into a functional of the electron density, *Phys. Rev. B:Condens. Matter Mater. Phys.*, 1988, **37**, 785–789.
32 K. Raghavachari, J. S. Binkley, R. Seeger and J. A. Pople, Self-Consistent Molecular Orbital Methods. 20. Basis set for correlated wave-functions, *J. Chem. Phys.*, 1980, **72**, 650–654.
33 M. J. Frisch, G. W. Trucks, H. B. Schlegel, G. E. Scuseria, M. A. Robb, J. R. Cheeseman, G. Scalmani, V. Barone, G. A. Petersson, H. Nakatsuji, X. Li, M. Caricato, A. V. Marenich, J. Bloino, B. G. Janesko, R. Gomperts, B. Mennucci, H. P. Hratchian, J. V. Ortiz, A. F. Izmaylov, J. L. Sonnenberg, D. Williams-Young, F. Ding, F. Lipparini, F. Egidi, J. Goings, B. Peng, A. Petrone, T. Henderson, D. Ranasinghe, V. G. Zakrzewski, J. Gao, N. Rega, G. Zheng, W. Liang, M. Hada, M. Ehara, K. Toyota, R. Fukuda, J. Hasegawa, M. Ishida, T. Nakajima, Y. Honda, O. Kitao, H. Nakai, T. Vreven, K. Throssell, J. A. Montgomery Jr, J. E. Peralta, F. Ogliaro, M. J. Bearpark, J. J. Heyd, E. N. Brothers, K. N. Kudin, V. N. Staroverov, T. A. Keith, R. Kobayashi, J. Normand, K. Raghavachari, A. P. Rendell, J. C. Burant, S. S. Iyengar, J. Tomasi, M. Cossi, J. M. Millam, M. Klene, C. Adamo, R. Cammi, J. W. Ochterski, R. L. Martin, K. Morokuma, O. Farkas, J. B. Foresman and D. J. Fox, *Gaussian, Inc.*, Wallingford CT, 2016.
34 X. Li and M. J. Frisch, Energy-represented DIIS within a hybrid geometry optimization method, *J. Chem. Theory Comput.*, 2006, **2**, 835–839.
35 K. N. Kudin, G. E. Scuseria and E. Cancès, A black-box self-consistent field convergence algorithm: One step closer, *J. Chem. Phys.*, 2002, **116**, 8255–8261.
36 *GaussView 6.0.16, Gaussian, Inc.*, Wallingford CT, 2016.
37 A. Borba, M. Albrecht, A. Gomez-Zavaglia, L. Lapinski, M. J. Nowak, M. A. Suhm and R. Fausto, Dimer formation in nicotinamide and picolinamide in the gas and condensed phases probed by infrared spectroscopy, *Phys. Chem. Chem. Phys.*, 2008, **10**(46), 7010–7021.
38 K. Wolinski, J. F. Hinton and P. Pulay, Efficient implementation of the gauge-independent atomic orbital method for NMR chemical shift calculations, *J. Am. Chem. Soc.*, 1990, **112**(23), 8251–8260.
39 J. R. Cheeseman, G. W. Trucks, T. A. Keith and M. J. Frisch, A comparison of models for calculating nuclear magnetic resonance shielding tensors, *J. Chem. Phys.*, 1996, **104**(14), 5497–5509.
40 M. E. Casida, C. Jamorski, K. C. Casida and D. R. Salahub, Molecular excitation energies to high-lying bound states from time-dependent density-functional response theory: Characterization and correction of the time-dependent local density approximation ionization threshold, *J. Chem. Phys.*, 1998, **108**, 4439–4449.
41 G. Scalmani, M. J. Frisch, B. Mennucci, J. Tomasi, R. Cammi and V. Barone, Geometries and properties of excited states in the gas phase and in solution: Theory and application of a time-dependent density functional theory polarizable continuum model, *J. Chem. Phys.*, 2006, **124**(9), 094107.
42 M. Cossi, V. Barone, R. Cammi and J. Tomasi, *Ab initio* study of solvated molecules: a new implementation of the polarizable continuum model, *Chem. Phys. Lett.*, 1996, **255**, 327–335.
43 J. Tomasi, B. Mennucci and R. Cammi, Quantum mechanical continuum solvation models, *Chem. Rev.*, 2005, **105**, 2999–3093.
44 D. A. McQuarrie, *Statistical Thermodynamics*, Harper & Row Publishers, New York, 1973.
45 G. Herzberg, *Molecular Spectra and Molecular Structure III*, D. Van Nostrand Company, Inc., New York, 1st edn, 1964.

46 G. Serdaroglu and S. Durmaz, DFT and statistical mechanics entropy calculations of diatomic and polyatomic molecules, *Indian J. Chem.*, 2010, **49**, 861–866.
47 T. Koopmans, Über die Zuordnung von Wellenfunktionen und Eigenwertenzu den Einzelnen Elektronen Eines Atoms, *Physica*, 1934, **1**, 104–113.
48 J. P. Perdew, R. G. Parr, M. Levy and J. L. Balduz, Density-Functional Theory for Fractional Particle Number: Derivative Discontinuities of the Energy, *Phys. Rev. Lett.*, 1982, **49**(23), 1691–1694.
49 J. F. Janak, Proof that $\partial E/\partial_{ni} = \varepsilon i_n$ density-functional theory, *Phys. Rev. B:Condens. Matter Mater. Phys.*, 1978, **18**(12), 7165–7168.
50 J. P. Perdew and M. Levy, Physical Content of the Exact Kohn-Sham Orbital Energies: Band Gaps and Derivative Discontinuities, *Phys. Rev. Lett.*, 1983, **51**(20), 1884–1887.
51 R. G. Parr and R. G. Pearson, Absolute hardness: companion parameter to absolute electronegativity, *J. Am. Chem. Soc.*, 1983, **105**, 7512–7516.
52 R. G. Pearson, Absolute electronegativity and hardness correlated with molecular orbital theory, *Proc. Natl. Acad. Sci. U. S. A.*, 1986, **83**, 8440–8441.
53 R. G. Parr, L. V. Szentpaly and S. Liu, Electrophilicity Index, *J. Am. Chem. Soc.*, 1999, **121**, 1922–1924.
54 J. L. Gazquez, A. Cedillo and A. Vela, Electrodonatingand Electroaccepting Powers, *J. Phys. Chem. A*, 2007, **111**(10), 1966–1970.
55 B. Gomez, N. V. Likhanova, M. A. Domínguez-Aguilar, R. Martínez-Palou, A. Vela and J. L. Gazquez, Quantum Chemical Study of the Inhibitive Properties of 2-Pyridyl-Azoles, *J. Phys. Chem. B*, 2006, **110**(18), 8928–8934.
56 A. Daina, O. Michielin and V. Zoete, SwissADME: a free web tool to evaluate pharmacokinetics, druglikeness and medicinal chemistry friendliness of small molecules, *Sci. Rep.*, 2017, **7**, 42717.
57 A. Daina, O. Michielin and V. Zoete, iLOGP: A Simple, Robust, and Efficient Description of n-Octanol/Water Partition Coefficient for Drug Design Using the GB/SA Approach, *J. Chem. Inf. Model.*, 2014, **54**(12), 3284–3301.
58 T. Cheng, Y. Zhao, X. Li, F. Lin, Y. Xu, X. Zhang, Y. Li and R. Wang, Computation of Octanol−Water Partition Coefficients by Guiding an Additive Model with Knowledge, *J. Chem. Inf. Model.*, 2007, **47**(6), 2140–2148.
59 S. A. Wildman and G. M. Crippen, Prediction of Physicochemical Parameters by Atomic Contributions, *J. Chem. Inf. Comput. Sci.*, 1999, **39**, 868–873.
60 C. A. Lipinski, F. Lombardo, B. W. Dominy and P. J. Feeney, Experimental and computational approaches to estimate solubility and permeability in drug discovery and development settings, *Adv. Drug Delivery Rev.*, 2001, **46**, 3–26.
61 https://www.silicos-it.be.
62 J. S. Delaney, ESOL: Estimating Aqueous Solubility Directly from Molecular Structure, *J. Chem. Inf. Comput. Sci.*, 2004, **44**, 1000–1005.
63 J. Ali, P. Camilleri, M. B. Brown, A. J. Hutt and S. B. Kirton, In Silico Prediction of Aqueous Solubility Using Simple QSPR Models: The Importance of Phenol and Phenol-like Moieties, *J. Chem. Inf. Model.*, 2012, **52**, 2950–2957.
64 A. K. Ghose, V. N. Viswanadhan and J. J. Wendoloski, A Knowledge-Based Approach in Designing Combinatorial or Medicinal Chemistry Libraries for Drug Discovery. 1. A Qualitative and Quantitative Characterization of Known Drug Databases, *J. Comb. Chem.*, 1999, **1**, 55–68.
65 D. F. Veber, S. R. Johnson, H.-Y. Cheng, B. R. Smith, K. W. Ward and K. D. Kopple, Molecular Properties That Influence the Oral Bioavailability of Drug Candidates, *J. Med. Chem.*, 2002, **45**, 2615–2623.
66 W. J. Egan, K. M. Merz Jr and J. J. Baldwin, Prediction of Drug Absorption Using Multivariate Statistics, *J. Med. Chem.*, 2000, **43**, 3867–3877.
67 I. Muegge, S. L. Heald and D. Brittelli, Simple Selection Criteria for Drug-like Chemical Matter, *J. Med. Chem.*, 2001, **44**(12), 1841–1846.
68 Y. C. Martin, A Bioavailability Score, *J. Med. Chem.*, 2005, **48**, 3164–3170.
69 M. Kalhor, Z. Vahedi and H. Gharoubi, Design of a new method for one-pot synthesis of 2-amino thiazoles using trichloroisocyanuric acid in the presence of a novel multi-functional and magnetically catalytic nanosystem: Ca/4-MePy-IL@ZY-Fe3O4, *RSC Adv.*, 2023, **13**, 9208–9221.
70 J. Safari, Z. Abedi-Jazini, Z. Zarnegar and M. Sadeghi, Nanochitosan: a biopolymer catalytic system for the synthesis of 2-aminothiazoles, *Catal. Commun.*, 2016, **77**, 108–112.
71 S. M. Ujwaldev, N. A. Harry, M. Neetha and G. Anilkumar, Novel synthesis of 2-Aminothiazoles *via* Fe(III)-Iodine-catalyzed Hantzsch-type condensation, *J. Heterocycl. Chem.*, 2021, **58**, 646–653.
72 Q. Zhang, J. Wu, Z. Pan, W. Zhanf and W. Zhou, A one-pot synthesis of 2-aminothiazoles *via* the coupling of ketones and thiourea using I2/dimethyl sulfoxide as a catalytic oxidative system, *J. Chem. Res.*, 2021, **45**, 89–94.
73 G. Serdaroğlu, Functionalized p-cymene and pyrazine derivatives: Physicochemical, ADMT, drug-likeness, and DFT studies, *Comput. Biol. Chem.*, 2025, **117**, 108434.
74 G. Serdaroğlu, N. Uludağ and E. Üstün, Advancing Pyrrole Synthesis through DDQ Catalysis: A Comprehensive Research Incorporating DFT, ADMT, and Molecular Docking Analysis, *ChemistrySelect*, 2024, **9**, e202303222.
75 A. Brahmia, L. Bejaoui, J. Rolicek, R. B. Hassen, G. Serdaroğlu and S. Kaya, Synthesis, crystal structure, Hirshfeld surface analysis and DFT calculations of 2,2,2-tribromo-1-(3,5-dibromo-2-hydroxyphenyl)ethanone, *J. Mol. Struct.*, 2022, **1248**, 131313.
76 G. Serdaroğlu and N. Uludağ, The electronic and spectroscopic investigation of (±)-Dasycarpidone, *Vib. Spectrosc.*, 2020, **111**, 103156.
77 G. Serdaroğlu, N. Uludag and E. Erçağ, Cyanomethylation of 2,3,4,9-tetrahydro-1H-carbazol-1-one based on using two different reagents: antioxidant activity and DFT studies, *J. Mol. Struct.*, 2022, **1253**, 132262.
78 N. Uludag, G. Serdaroğlu, P. Sugumar, P. Rajkumar, N. Colak and Er. Ercag, Synthesis of thiophene

derivatives: Substituent effect, antioxidant activity, cyclic voltammetry, molecular docking, DFT, and TD-DFT calculations, *J. Mol. Struct.*, 2022, **1257**, 132607.

79 G. Serdaroğlu, N. Uludag, N. Colak and P. Rajkumar, Nitrobenzamido substitution on thiophene-3-carboxylate: Electrochemical investigation, antioxidant activity, molecular docking, DFT calculations, *J. Mol. Struct.*, 2023, **1271**, 134030.

80 G. Serdaroğlu, N. Uludag, P. Sugumar and P. Rajkumar, (-)-Tubifolidine as strychnos indole alkaloid: Spectroscopic charactarization (FT-IR, NMR, UV-Vis), antioxidant activity, molecular docking, and DFT studies, *J. Mol. Struct.*, 2021, **1244**, 130978.

81 G. Serdaroğlu, N. Uludağ, E. Üstün, G. Erten and N. Çolak, Design, synthesis, DNA, and BSA-binding of 5-mercapto-1,3,4-thiadiazol and 5-methylisoxazol derivatives: DFT, Molecular dockings, ADMET, and drug-likeness profiles, *J. Mol. Struct.*, 2026, **1351**, 144183.

82 G. Serdaroğlu, N. Uludag, E. Üstün and N. Colak, A novel series of tetrahydrothieno [2,3-c] pyridin-2-yl derivatives: fluorescence spectroscopy and BSA binding, ADMET properties, molecular docking, and DFT studies, *New J. Chem.*, 2023, **47**(25), 11945–11963.

83 R. Toplak, N. Lah, J. Volmajer, I. Leban and M. L. A. Marechal, 2-Amino-thiazole and 2-amino-thiazolinone derivatives, *Acta Crystallogr., Sect. C:Cryst. Struct. Commun.*, 2003, **59**, o502–o505, DOI: 10.1107/S0108270103015580.

84 R. A. Azzam, G. H. Elgemeie, R. E. Elsayed and P. G. Jones, Crystal structure of *N*′-[2-(benzo[d]thiazol-2-yl)acet-yl]-4-methyl-benzene-sulfono-hydrazide, *Acta Crystallogr., Sect. E:Crystallogr. Commun.*, 2017, **73**, 1041–1043.

85 C. A. Lipinski, F. Lombardo, B. W. Dominy and P. J. Feeney, Experimental and computational approaches to estimate solubility and permeability in drug discovery and development settings, *Adv. Drug Delivery Rev.*, 2012, **64**, 4–17.

86 ADMETlab 3.0.

87 A. Daina and V. Zoete, A BOILED-Egg To Predict Gastrointestinal Absorption and Brain Penetration of Small Molecules, *ChemMedChem*, 2016, **11**, 1117.

88 S. Soriano-Meseguer, E. Fuguet, A. Port and M. Rosés, Optimization of Experimental Conditions for Skin-PAMPA Measurements, *ADMET DMPK*, 2020, **8**(1), c16–c28.

89 R. Junejo, N. S. Jalbani, S. Kaya, G. Serdaroglu, S. Şimşek and S. Memon, Experimental and DFT Modeling Studies for the Adsorptive Removal of Reactive Dyes from Wastewater, *Sep. Sci. Technol.*, 2021, **57**(3), 339–353.

90 G. Serdaroğlu, A DFT study of determination of the reactive sites of the acetylcholine and its agonists: In the gas phase and dielectric medium, *Int. J. Quantum Chem.*, 2011, **111**(10), 2464–2475.

91 L. G. Ferreira, R. N. Dos Santos, G. Oliva and A. D. Andricopulo, Molecular docking and structure-based drug design strategies, *Molecules*, 2015, **20**(7), 13384–13421.

92 U. Tutar, C. Celik, E. Üstün, N. Özdemir, N. Şahin, D. Semeril and İ. Özdemir, Benzimidazol-2-ylidene silver complexes: Synthesis, characterization, antimicrobial and antibiofilm activities, molecular docking and theoretical investigations, *Inorganics*, 2023, **11**(10), 385.

93 S. J. Modi and V. M. Kulkarni, Vascular endothelial growth factor receptor (VEGFR-2)/KDR inhibitors: medicinal chemistry perspective, *Med. Drug Discovery*, 2019, **2**, 100009.

94 V. Joukov, K. Pajusola, A. Kaipainen, D. Chilov, I. Lahtinen, E. Kukk and K. Alitalo, A novel vascular endothelial growth factor, VEGF-C, is a ligand for the Flt4 (VEGFR-3) and KDR (VEGFR-2) receptor tyrosine kinases, *EMBO J.*, 1996, **15**(2), 290–298.

95 S. M. Al-Hazmy, M. O. Zouaghi, J. N. Al-Johani, Y. Arfaoui, R. Al-Ashwal, B. Hammami and N. Hamdi, Chemosensing properties of coumarin derivatives: promising agents with diverse pharmacological properties, docking and DFT investigation, *Molecules*, 2022, **27**(18), 5921.

96 G. Serdaroğlu, N. Şahin, S. Şahin-Bölükbaşı and E. Üstün, Novel Ag (I)-NHC complex: Synthesis, *in vitro* cytotoxic activity, molecular docking, and quantum chemical studies, *ZNC*, 2022, **77**(1–2), 21–36.

97 P. Mamta and A. Chaudhary, Synthesis, spectroscopic elucidation, density functional theory calculation, and molecular docking studies of a novel series of tetradentate macrocyclic Schiff base ligands and their Zn(II) complexes and investigations of their antimicrobial, anti-inflammatory, and anticancer activities, *App. Organomet. Chem.*, 2024, **38**(2), e7330.

98 W. Yue, J. P. Wang, Y. Li, P. Fan, G. Liu, N. Zhang and R. Santen, Effects of estrogen on breast cancer development: Role of estrogen receptor independent mechanisms, *Indian J. Chem.*, 2010, **127**(8), 1748–1757.

99 P. H. Kumar, M. Rambabu, V. Vijayakumar and S. Sarveswari, Palladium-Mediated Synthesis of 2-([biphenyl]-4-yloxy) quinolin-3-carbaldehydes through Suzuki–Miyaura Cross-Coupling and Their *in Silico* Breast Cancer Studies on the 3ERT Protein, *ACS Omega*, 2023, **8**(13), 11806–11812.

100 D. Sarkar and A. K. Maiti, Virtual screening and molecular docking studies with organosulfur and flavonoid compounds of garlic targeting the estrogen receptor protein for the therapy of breast cancer, *Biointerface Res. Appl. Chem.*, 2023, **13**(1), 49.

101 R. Sehrawat, P. Rathee, P. Rathee, S. Khatkar, E. K. Akkol, A. Khatkar and E. Sobarzo-Sánchez, In silico design of novel bioactive molecules to treat breast cancer with chlorogenic acid derivatives: a computational and SAR approach, *Front. Pharmacol.*, 2023, **14**, 1266833.

102 F. P. Guengerich, Reactions and significance of cytochrome P-450 enzymes, *J. Biol. Chem.*, 1991, **266**(16), 10019–10022.

103 S. Haidar, P. B. Ehmer, S. Barassin, C. Batzl-Hartmann and R. W. Hartmann, Effects of novel 17α-hydroxylase/C17, 20-lyase (P450 17, CYP 17) inhibitors on androgen biosynthesis *in vitro* and *in vivo*, *JSBMB*, 2003, **84**(5), 555–562.

104 S. A. Dhawale, P. Bhosle, S. Mahajan, G. Patil, S. Gawale, M. Ghodke and A. Ansari, Dual targeting in prostate cancer with phytoconstituents as a potent lead:

a computational approach for novel drug discovery, *J. Biomol. Struct. Dyn.*, 2024, **42**(17), 8906–8919.

105 M. Behzad, L. Ghasemi, M. Dusek and M. Kučeráková, Computer-Aided Investigation of Anticancer Properties of New Mixed-Ligand Cu (II) Complexes of an Unsymmetrical Schiff Base Ligand by ADMET and Molecular Docking: Comparison With Chemical Drugs and Curcumin, *App. Organomet. Chem.*, 2025, **39**(1), e7918.

106 F. Tajiani, S. Ahmadi, S. Lotfi, P. Kumar and A. Almasirad, In-silico activity prediction and docking studies of some flavonol derivatives as anti-prostate cancer agents based on Monte Carlo optimization, *BMC Chem.*, 2023, **17**(1), 87.

107 N. Lu and C. J. Malemud, Extracellular signal-regulated kinase: a regulator of cell growth, inflammation, chondrocyte and bone cell receptor-mediated gene expression, *Int. J. Mol. Sci.*, 2019, **20**(15), 3792.

108 X. Pan, J. Pei, A. Wang, W. Shuai, L. Feng, F. Bu and L. Ouyang, Development of small molecule extracellular signal-regulated kinases (ERKs) inhibitors for cancer therapy, *Acta Pharm. Sin. B*, 2022, **12**(5), 2171–2192.

109 J. Zhao, T. Zhang, Y. Liang, H. Zou and J. Zhang, Inhibitory activities of 20 (R, S)-protopanaxatriol against epidermal growth factor receptor tyrosine kinase, *Food Chem. Toxicol.*, 2021, **155**, 112411.

110 Y. Niu, X. Yao and H. Ji, Importance of protein flexibility in ranking ERK2 Type I 1/2 inhibitor affinities: a computational study, *RSC Adv.*, 2019, **9**(22), 12441–12454.